

# An H<sub>2</sub>O–CO<sub>2</sub> mixed fluid saturation model compatible with rhyolite-MELTS

Mark S. Ghiorso<sup>1</sup> · Guilherme A. R. Gualda<sup>2</sup>

Received: 6 November 2013 / Accepted: 14 April 2015 / Published online: 5 June 2015  
© Springer-Verlag Berlin Heidelberg 2015

**Abstract** A thermodynamic model for estimating the saturation conditions of H<sub>2</sub>O–CO<sub>2</sub> mixed fluids in multi-component silicate liquids is described. The model extends the capabilities of rhyolite-MELTS (Gualda et al. in J Petrol 53:875–890, 2012a) and augments the water saturation model in MELTS (Ghiorso and Sack in Contrib Mineral Petrol 119:197–212, 1995). The model is internally consistent with the fluid-phase thermodynamic model of Duan and Zhang (Geochim Cosmochim Acta 70:2311–2324, 2006). It may be used independently of rhyolite-MELTS to estimate intensive variables and fluid saturation conditions from glass inclusions trapped in phenocrysts. The model is calibrated from published experimental data on water and carbon dioxide solubility, and mixed fluid saturation in silicate liquids. The model is constructed on the assumption that water dissolves to form a hydroxyl melt species, and that carbon dioxide both a molecular species and a carbonate ion, the latter complexed with calcium. Excess enthalpy interaction terms in part compensate for these simplistic assumptions regarding speciation. The model is restricted to *natural composition liquids* over the pressure range 0–3 GPa. One characteristic of the model is that fluid saturation isobars at pressures greater than ~100 MPa always display

a maximum in melt CO<sub>2</sub> at nonzero H<sub>2</sub>O melt concentrations, regardless of bulk composition. This feature is universal and can be attributed to the dominance of hydroxyl speciation at low water concentrations. The model is applied to four examples. The first involves estimation of pressures from H<sub>2</sub>O–CO<sub>2</sub>-bearing glass inclusions found in quartz phenocrysts of the Bishop Tuff. The second illustrates H<sub>2</sub>O and CO<sub>2</sub> partitioning between melt and fluid during fluid-saturated equilibrium and fractional crystallization of MORB. The third example demonstrates that the position of the quartz–feldspar cotectic surface is insensitive to melt CO<sub>2</sub> contents, which facilitates geobarometry using phase equilibria. The final example shows the effect of H<sub>2</sub>O and CO<sub>2</sub> on the crystallization paths of a high-silica rhyolite composition representative of the late-erupted Bishop Tuff. Software that implements the model is available at ofm-research.org, and the model is incorporated into the latest version (1.1+) of rhyolite-MELTS.

**Keywords** Mixed fluid saturation · Silicate melts · Thermodynamics · MELTS

## Introduction and previous work

The presence of a fluid phase in a magmatic assemblage has an essential influence on the phase relations, elemental partitioning, and material properties of the system. The viscosity, density, and compressibility of a magma body are all critically dependent on the concentration of dissolved fluid (Lange 1994; Ochs and Lange 1997; Giordano et al. 2008). The partitioning of trace elements between minerals and melt can be markedly different if a fluid phase coexists with the assemblage (Spera et al. 2007). The saturation condition for a fluid phase coexisting with silicate melt is

Communicated by Gordon Moore.

**Electronic supplementary material** The online version of this article (doi:10.1007/s00410-015-1141-8) contains supplementary material, which is available to authorized users.

✉ Mark S. Ghiorso  
ghiorso@ofm-research.org

<sup>1</sup> OFM-Research, Seattle, WA 98115, USA

<sup>2</sup> Earth and Environmental Sciences, Vanderbilt University, Nashville, TN 37235, USA

a strong function of the proportion of  $\text{H}_2\text{O}$  to  $\text{CO}_2$  in that phase. This is because of the compositionally dependent differential solubility of  $\text{H}_2\text{O}$ - and  $\text{CO}_2$ -rich fluids in silicate liquids and the strong partitioning of the two volatile components between melt and fluid. It is the nature of this partitioning that motivates the application of mixed volatile phase saturation to the interpretation of magmatic pre-eruptive conditions from the  $\text{H}_2\text{O}$  and  $\text{CO}_2$  contents of glass inclusions in magmatic minerals (Moore 2008). The importance of this partitioning and the role it plays in interpreting the dynamical evolution of magma bodies has instigated an impressive number of experimental studies characterizing volatile saturation conditions and the physics and chemistry of the mechanism of fluid saturation. In turn, the experimental studies have spawned a number of models aimed at systematizing these observations in order to provide a predictive framework for the interpretation of data on natural rock samples.

The aim of this paper is to present a new thermodynamic model for mixed  $\text{H}_2\text{O}$ – $\text{CO}_2$  fluid saturation in natural silicate melts. The model presented is compatible with the computational frameworks and thermodynamic data/model collections embodied in rhyolite-MELTS (Gualda et al. 2012a) and MELTS (Ghiorso and Sack 1995). Consequently, it may be used in conjunction with these computational packages to model the effects of mixed fluid saturation on liquid–solid phase relations in magmatic systems under crustal pressure ( $P$ )–temperature ( $T$ ) conditions. Internal consistency with MELTS and rhyolite-MELTS discriminates the model presented here from the work of Duan (2014), Papale (1997, 1999), Papale et al. (2006), Moore et al. (1998), Dixon et al. (1995), Newman and Lowenstern (2002), and others (see Table 3 of Moore 2008). Additionally, the described model extends the calibration database of Papale et al. (2006) and improves upon the underlying theoretical formulation for activity composition relations of the  $\text{H}_2\text{O}$  component in the melt (after Ghiorso et al. 1983), as well as implementing a more robust and extensible model for the thermodynamic properties of the fluid phase (following Duan and Zhang 2006; this fluid model is also adopted by Duan 2014).

We proceed by first describing the model and the underlying objectives of its formulation and then discuss the calibration database, and finally the mechanics and compromises of calibration. The paper ends with applications aimed to (1) illustrate the use of the model to estimate fluid saturation in basaltic and rhyolitic bulk compositions; (2) demonstrate the use of the model coupled with rhyolite-MELTS to show the evolution of fluid saturation and  $\text{CO}_2$ – $\text{H}_2\text{O}$  partitioning during equilibrium and fractional crystallization of basalt and rhyolite. In Electronic Supplementary Materials (ESM), an Appendix is provided that enumerates the details of both the fluid and melt models and discusses

the method of parameter optimization used for the calibration of the model to experimental data.

An extended version of rhyolite-MELTS and software for performing solubility and partitioning calculations based on the model presented here is available at the URL [ofm-research.org](http://ofm-research.org).

## The model

Our objective is to formulate a thermodynamic model for mixed  $\text{H}_2\text{O}$ – $\text{CO}_2$  fluid saturation that is compatible with MELTS (Ghiorso and Sack 1995) and rhyolite-MELTS (Gualda et al. 2012a). Effectively, this means that we seek a model that can be applied under crustal to supercrustal  $T$ - and  $P$ -conditions (600–1400 °C, 0–3 GPa) and that is internally consistent with the “anhydrous” silicate–liquid model of MELTS, which is identical to that in rhyolite-MELTS. The former restriction does not substantially limit the application of the model because effectively this pressure range encompasses the database of mixed volatile saturation experiments (see below). The latter restriction gives us the advantage that once calibrated from solubility data, estimates of the effects of dissolved volatiles on solid–liquid phase relations can be assessed in an internally consistent manner. The model we seek, however, will, by design, not be compatible with pMELTS (Ghiorso et al. 2002), nor will it be intended to model  $\text{CO}_2$ -rich fluid equilibria under mantle-like conditions at  $P > 3$  GPa. In our view, the available experimental data are simply not extensive enough to provide a means of calibration in the higher-pressure regime.

MELTS and rhyolite-MELTS contain identical thermodynamic descriptions for the solubility of a pure  $\text{H}_2\text{O}$  component fluid phase. The formulation is based upon a configurational entropy model for dissolved  $\text{H}_2\text{O}$  in the melt originally devised by Ghiorso et al. (1983), which is built upon the formulations of Nicholls (1980) and Burnham and Davis (1974). Standard-state<sup>1</sup> thermodynamic properties of the  $\text{H}_2\text{O}$  component in the melt are taken in part from the equation of state (EOS) of Burnham et al. (1969), with partial molar entropy and enthalpy determined from model calibration. Thermodynamic properties of the water phase in MELTS were adopted from Haar et al. (1984) for pressures below 1 GPa and from Helgeson and Kirkham (1974) at higher pressures.

When attempting to extend MELTS to include a mixed fluid solubility model, four principal questions emerge: (1) Will the configurational entropy model for the melt  $\text{H}_2\text{O}$

<sup>1</sup> Throughout this paper for the melt phase: Unit activity of the pure substance at any  $T$  and  $P$ .

component need modification? (2) What model will be adopted to describe thermodynamic properties of the mixed fluid phase? (3) What standard-state properties for melt component end members are optimal? and (4) Will excess free energy parameters involving H<sub>2</sub>O inherited from the MELTS model require modification?

In MELTS, the configurational entropy model for the H<sub>2</sub>O component dissolved in silicate liquid is based on the physical assumption that H<sub>2</sub>O dissociates completely to hydroxyl units in the melt phase. This assumption motivates the relation  $a_{\text{H}_2\text{O}} \approx X_{\text{H}_2\text{O}}^2$ , where  $a$  denotes the activity and  $X$  the mole fraction of dissolved water. This relationship implies (Ghiorso et al. 1983):

$$\hat{S}^{\text{conf}} = -R \sum_{i=1}^{\text{anhydrous components}} X_i \ln X_i - 2RX_{\text{H}_2\text{O}} \ln X_{\text{H}_2\text{O}} - R(1 - X_{\text{H}_2\text{O}}) \ln(1 - X_{\text{H}_2\text{O}}) \quad (1)$$

for the molar configurational entropy of mixing as a consequence of the requirement of the equality of cross-partial compositional derivatives of any thermodynamic state function (Prigogine and Defay 1954). Importantly, a necessary consequence of (1) is that for any “anhydrous” melt component:  $a_i \approx X_i(1 - X_{\text{H}_2\text{O}})$ . The MELTS configurational entropy model does not include energetic contributions that might arise from partitioning of dissolved water into hydroxyl and molecular species (Stolper 1982). This is an apparent deficiency that may impact the ability to model water solubility experimental data over the whole range of compositions, temperatures, and pressures of interest. Speciation was not included in MELTS because the additional complexity would necessitate calibration of excess Gibbs free energy parameters for *both* hydroxyl and molecular water interactions with “anhydrous” melt species, effectively doubling the number of model parameters, and the experimental database available at the time of calibration did not warrant such an extension (Ghiorso and Sack 1995). This simplification must be revisited and assessed in light of the more comprehensive calibration data set assembled for the present analysis.

The pure water phase thermodynamic models utilized in MELTS are unsuitable for the mixed fluid models required here because they cannot readily be extended into the H<sub>2</sub>O–CO<sub>2</sub> join with its complex and highly non-ideal solution properties. Papale et al. (2006) used the thermodynamic model of Kerrick and Jacobs (1981), which is a modified Redlick–Kwong formulation for the H<sub>2</sub>O–CO<sub>2</sub> system. Along with Duan (2014), we choose the model of Duan and Zhang (2006; see ESM Appendix to this paper). This more recent formulation is based on a virial expansion EOS and is therefore more readily extensible to more complex fluids (e.g., plus CH<sub>4</sub>, SO<sub>2</sub>). Their model reproduces well

the extensive post-1981 data sets on mixing relations across the binary join (Duan and Zhang 2006, their Table 1) and is calibrated in part on first principle MD results that facilitate the extrapolation of the model to elevated temperatures (to 2300 °C) and pressures (to 10 GPa). Most importantly, the model of Duan and Zhang (2006) retrieves properties for water that are consistent with Haar et al. (1984) and Helgeson and Kirkham (1974) over the  $P$ – $T$  range of interest here.

The EOS for the dissolved H<sub>2</sub>O component in silicate liquids that is used in MELTS is adapted from the work of Nicholls (1980) and is ultimately attributable to Burnham et al. (1969). This EOS is a volume explicit polynomial in  $T$  and  $P$  with 15 parameters. The data for this EOS are derived from the determinations of the partial molar volume of H<sub>2</sub>O in albite composition liquids. Ochs and Lange (1997) reevaluated these experimental results, adopting a smaller reference volume for dissolved water in the melt and found that the  $T$ – $P$  dependence of the data could be adequately recovered, better interpolated, and better extrapolated using a three-parameter EOS:

$$\bar{v}_{\text{H}_2\text{O},T,P}^{\circ} = \bar{v}_{\text{H}_2\text{O},1400\text{ K},1\text{ bar}}^{\circ} + \frac{\partial \bar{v}_{\text{H}_2\text{O}}^{\circ}}{\partial T}(T - 1400) + \frac{\partial \bar{v}_{\text{H}_2\text{O}}^{\circ}}{\partial P}(P - 1) \quad (2)$$

Here,  $\bar{v}_{\text{H}_2\text{O}}^{\circ}$  is the standard-state partial molar volume of H<sub>2</sub>O dissolved in the melt. In this paper, we will adopt the Ochs and Lange (1997) expression in substitute for that obtained by Burnham et al. (1969) for the recalibration of the water solubility model in MELTS. The same course of action was followed with success in developing the water solubility calibration in pMELTS (Ghiorso et al. 2002).

## Calibration data

Duan (2014), Papale et al. (2006), and Moore (2008) summarize experimental data available from the literature to assess the solubility of H<sub>2</sub>O–CO<sub>2</sub> fluids in silicate liquids and the differential partitioning of H<sub>2</sub>O and CO<sub>2</sub> between the two phases. We have based our calibration database on their summaries, adding more recent data where available. Data are used only if liquid and fluid compositions as well as temperature and pressure are reported in the source or can be reliably estimated from provided experimental descriptions or metadata. Experiments that produced solid phases were discarded unless analyses of quenched glass are reported. In mixed H<sub>2</sub>O–CO<sub>2</sub> fluid saturation experiments, analytical measurements of the two volatile components in both quenched glass and fluid are required for inclusion in the data set. In addition, we have excluded the CO<sub>2</sub> solubility measurements from the literature where the analysis of dissolved carbon was made using beta-track

**Table 1** Data sources utilized in model calibration

References	Number of experimental constraints		
	H <sub>2</sub> O fluid experiments	CO <sub>2</sub> fluid experiments	Mixed H <sub>2</sub> O–CO <sub>2</sub> fluid experiments
Barclay et al. (1998)	1		
Behrens (1995)	56		
Behrens and Jantos (2001)	37		
Behrens et al. (2001)	50		
Behrens et al. (2004a)			12
Behrens et al. (2009)	21		20
Benne and Behrens (2003)	41		
Berndt et al. (2002)	9		
Bezmen et al. (1991)	1		
Blank et al. (1993)			7
Blatter and Carmichael (2001)	2		
Botcharnikov et al. (2005a)	1		
Botcharnikov et al. (2005b)	3		9
Botcharnikov et al. (2006)	2		21
Botcharnikov et al. (2007)	3		3
Brey (1976)		1	
Brooker et al. (1999)		27	
Brooker et al. (2001)		10	
Burnham and Jahns (1962)	57		
Carroll and Blank (1997)	20		
Di Matteo et al. (2004)	15		
Dingwell et al. (1984)	12		
Dingwell et al. (1997)	17		
Dixon et al. (1995)	6		9
Feig et al. (2006)	1		
Gaillard et al. (2003)	11		
Gerke and Kilinc (1992)	1		
Grove et al. (1997)	2		
Hamilton and Oxtoby (1986)	50		
Hamilton et al. (1964)	11		
Hammer et al. (2002)	1		
Holtz et al. (1992)	28		
Holtz et al. (1995)	87		
Holtz et al. (2000)	27		
Iacono-Marziano et al. (2008)	1		
Iacono-Marziano et al. (2012)	6		23
Iacovino et al. (2013)			15
Jakobsson (1997)			8
Kennedy et al. (1962)	13		
Khitarov et al. (1963)	18		
Khitarov et al. (1968)	9		
King and Holloway (2002)		1	4
Kogarko et al. (1977)	12		
Kohn et al. (1989)	5		
Larsen and Gardner (2004)	5		
Lesne et al. (2011a)			34
Lesne et al. (2011b)			13

**Table 1** continued

References	Number of experimental constraints		
	H <sub>2</sub> O fluid experiments	CO <sub>2</sub> fluid experiments	Mixed H <sub>2</sub> O–CO <sub>2</sub> fluid experiments
Lesne et al. (2011c)	25		25
Liu et al. (2005)	21		
Mangan and Sisson (2000)	1		
Martel et al. (1998)	5		
Mattey (1991)		5	
Mattey et al. (1990)		13	
McMillan et al. (1986)	9		
Medard and Grove (2008)	9		
Métrich and Rutherford (1998)	10		
Moore and Carmichael (1998)	12		
Moore et al. (1998)	41		
Moore et al. (2008)	1		
Morizet et al. (2002)		30	
Morizet et al. (2010)			10
Mysen and Cody (2004)	53		
Ohlhorst et al. (2001)	6		
Orlova (1962)	21		
Oxtoby and Hamilton (1978)	52		
Paillat et al. (1992)	9		
Pan et al. (1991)		15	
Pawley et al. (1992)		5	
Persikov (1974)	15		
Pineau et al. (1998)	7		
Rai et al. (1983)		6	
Roach (2005)	5	5	
Romano et al. (1996)	40		
Schmidt and Behrens (2008)	69		
Schmidt et al. (1999)	4		
Shaw (1963)	2		
Shishkina et al. (2010)	7		27
Shishkina et al. (2014)	4		33
Silver et al. (1990)	45		
Tamic et al. (2001)	4		34
Thibault and Holloway (1994)		16	
Vetere et al. (2011)	5		16
Vetere et al. (2014)	4		16
Watson (1979)	2		
Wilke et al. (2002)	6		
Yamashita (1999)	15		
Yoder (1965)	1		
Total	1152	134	339

methods (e.g., Mysen et al. 1974). These measurements yield results that contradict several other experimental studies, specifically in the pressure dependence of the solubility relations. While Papale et al. (2006) did include these beta-track experiments as constraints for his model,

Duan (2014) chose not to do so, and in comparison with Papale, this resulted in fewer pressure-dependent model parameters for CO<sub>2</sub> solubility. We follow Duan's example and exclude beta-track measurements from our calibration data set.

Data sources are tabulated in Table 1, corresponding to fluid saturation experiments involving water, carbon dioxide, and mixed fluids. All the data sources listed have been entered into LEPR (lepr.ofm-research.org, Hirschmann et al. 2008), and a combined data file that is compliant with the LEPR schema is available at ofm-research.org. For all iron-bearing experiments, the ferric and ferrous iron contents of the melt are estimated using Kress and Carmichael (1988). Figures 1 and 2 display visualizations of the composition, temperature, and pressure ranges of the three data sets. It is important to note that there is minimal overlap in  $T$ - and  $P$ -spaces for the  $H_2O$  and  $CO_2$  solubility data sets (Fig. 2d). In part, this is due to practical considerations of experimental design derived from the limited solubility of  $CO_2$  in silicate liquids at low pressures. The lack of overlap, however, has certain consequences for parameter calibration, as we discuss below, and will motivate our decision to utilize both the pure  $CO_2$  solubility experiments and the fluid saturation experiments together for the calibration of the energetic properties of  $CO_2$  in the melt. The majority of data (1152 cases) constrain water solubility, and despite the relevance and intense interest in mixed volatile solubility relations and partitioning, there are a smaller number (339) of mixed volatile experiments that in turn span a more restricted portion of the composition space of natural liquids (Fig. 1c). It is especially important to note that very little data are available (and only water solubility results) at temperatures below 800 °C (Fig. 1), which means that the application of any model calibrated from these data to natural phase assemblages involving quartz + sanidine + plagioclase + fluid will involve extrapolation to lower temperatures (c.f., Johannes and Holtz 1996).

### Assessment of the MELTS water solubility model and recalibration

The first task is to assess the suitability of the MELTS water solubility model against the calibration database. We perform this assessment in two ways. First, we calculate from experimentally reported temperatures and pressures and the thermochemical model of Duan and Zhang (2006) the chemical potential of water ( $\mu_{H_2O}^o$ , see ESM Appendix). Concurrently, utilizing the activity composition relations for  $H_2O$ -bearing silicate liquids from MELTS, we calculate from the experimentally reported liquid compositions and water contents the chemical potential of  $H_2O$  in the silicate liquid ( $\mu_{H_2O}^{melt}$ ). The difference between these two quantities  $\Delta\mu_{H_2O}^{residual} = \mu_{H_2O}^{melt} - \mu_{H_2O}^o$ , is an energetic residual that describes the degree of misfit between model and data. The second way we can assess the applicability of the MELTS water model to the calibration data set is to calculate the dissolved water content of the experimental silicate liquid

**Fig. 1** Bulk compositions of calibration data sets projected onto the alkali-silica rock classification diagram of Le Bas et al. (1986). **a** Water solubility experiments (see accompanying legend and Table 1), **b** carbon dioxide solubility experiments (see Table 1), **c** saturated mixed  $H_2O$ - $CO_2$  fluid experiments (see Table 1). Reference compositions are plotted: Fo =  $Mg_2SiO_4$ , Di =  $CaMgSi_2O_6$ , Ab =  $NaAlSi_3O_8$ , Jd =  $NaAl_2Si_2O_6$ , Ne =  $NaAlSiO_4$

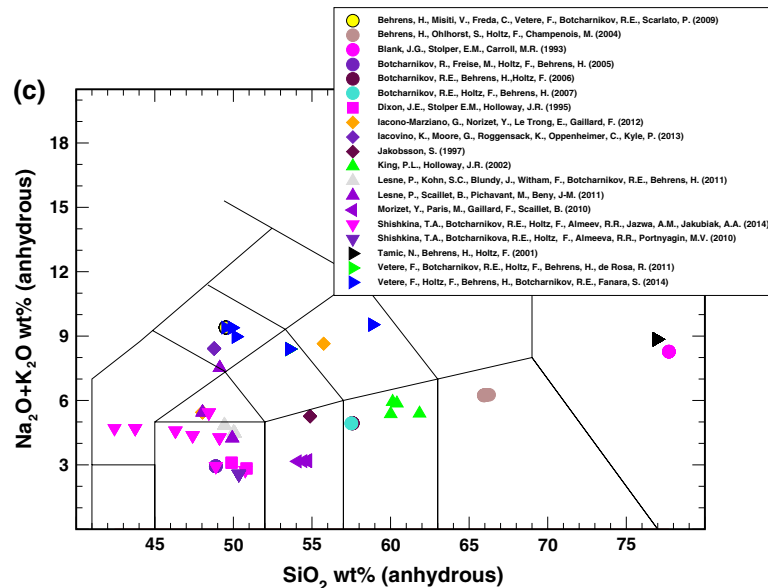
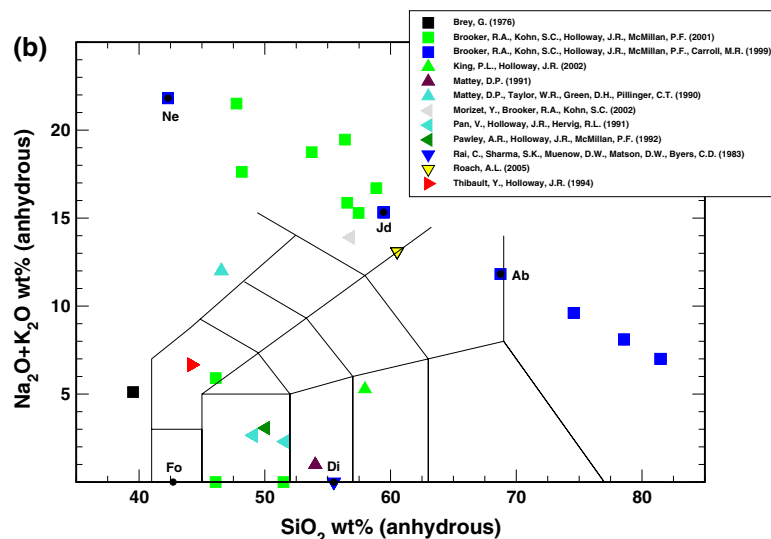
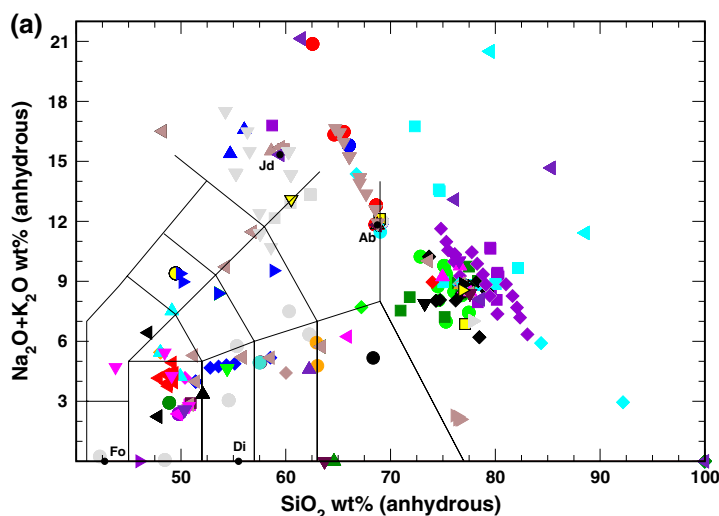
from the identity  $\mu_{H_2O}^{melt} = f(\text{wt}\%_{\text{model-}H_2O}) = \mu_{H_2O}^o$  and compare  $\text{wt}\%_{\text{model-}H_2O}$  to  $\text{wt}\%_{\text{experiment-}H_2O}$ . This comparison offers a direct assessment of how well the model reproduces a directly measured experimental quantity.

Assessment of the water solubility data set against the MELTS water model is shown in Figs. 3, 4, and 5. Figure 3a, b examines energetic residuals as a function of melt water concentration. In Fig. 3b, we have culled the data to only plot experiments performed on *natural*<sup>2</sup> composition melts; this data filtering is consistent with the compositional range over which the MELTS calibration, which is based on both anhydrous and water-bearing experiments, is applicable. The average statistical uncertainty of the entire data set scatters about zero, with standard deviation on the order of 3 kJ/mol (Fig. 3a). The natural data set has a much tighter distribution of residuals, but the mean is skewed to negative values, and close examination reveals that poorest recovery occurs in more alkali-rich bulk compositions. This is not surprising, as these compositions represent the furthest extrapolation from the original MELTS water calibration, which was based on a subset of data from Burnham and Jahns (1962, five experiments), Hamilton et al. (1964, 11 experiments), Khitarov et al. (Khitarov et al. 1963, 1968, 12 experiments), and a small number (119 experiments) of multiply saturated (solid + fluid) phase equilibrium studies (Ghiorso and Sack 1995, their Table A2) spanning the composition range of basalt to rhyolite, the pressure range 10–500 MPa, and the temperature interval 670–1150 °C.

Figure 4 shows a visual assessment of  $\text{wt}\%_{\text{model-}H_2O}$  versus  $\text{wt}\%_{\text{experiment-}H_2O}$  for the entire calibration data set (Fig. 4a) and the subset of natural compositions (Fig. 4b). The first thing to notice is that errors in energetic residuals ( $\Delta\mu_{H_2O}^{residual} = \mu_{H_2O}^{melt} - \mu_{H_2O}^o$ , Fig. 3) do not translate uniformly to errors in model  $H_2O$  concentrations. This is because the chemical potential of water in the melt is to first order a function of the logarithm of water mole fraction. This logarithmic dependence means that the same uniform error in energetic residual requires a larger compensation in melt water mole fraction to zero that residual at high concentrations of water when

<sup>2</sup> Through this paper, we define a *natural* composition as one that contains finite concentrations of the oxides  $SiO_2$ ,  $Al_2O_3$ ,  $FeO$ ,  $MgO$ ,  $CaO$ , and one of either  $Na_2O$  or  $K_2O$ .





- Barclay, J., Rutherford, M.J., Carroll, M.R., Murphy, M.D., Devine, J.D., Gardner, J., Sparks, R.S.J. (1998)
- Behrens, H. (1995)
- Behrens, H., Jantos, N. (2001)
- Behrens, H., Meyer, M., Holtz, F., Benne, D., Nowak, M. (2001)
- Behrens, H., Misilli, V., Freda, C., Vetere, F., Botcharnikov, R.E., Scariato, P. (2009)
- Benne, D., Behrens, H. (2003)
- Berndt, J., Liebske, C., Holtz, F., Freise, M., Nowak, M., Ziegenbein, D., Hurlkuck, W., Koepke, J. (2002)
- Bezmen, I.I., Zharikov, V.A., Epelbaum, M.B., Zavelevsky, V.O., Dikov, Y.P., Suk, N.I., Koshemchuk, S.K. (1991)
- Blatter, D.W., Carmichael, I.S.E. (2001)
- Botcharnikov, R., Freise, M., Holtz, F., Behrens, H. (2005)
- Botcharnikov, R.E., Behrens, H., Holtz, F. (2006)
- Botcharnikov, R.E., Holtz, F., Behrens, H. (2007)
- Botcharnikov, R.E., Koepke, J., Holtz, F., McCammon, C., Wilke, M. (2005)
- Burnham, C.W., Jahn, R.H. (1962)
- Carroll, M.R., Blank, J.G. (1997)
- Di Matteo, V., Carroll, M.R., Behrens, H., Vetere, F., Brooker, R.A. (2004)
- Dingwell, D.B., Harris, D.M., Scarfe, C.M. (1984)
- Dingwell, D.B., Holtz, F., Behrens, H. (1997)
- Dixon, J.E., Stolper, E.M., Holloway, J.R. (1995)
- Feig, S.T., Koepke, J., Snow, J.E. (2006)
- Gaillard, F., Pichavant, M., Scaillet, B. (2003)
- Gerke, T.L., Kilinc, A.I. (1992)
- Grove, T.L., Donnelly-Nolan, J.M., Housh, T. (1997)
- Hamilton, D.L., Burnham, C.W., Osborn, E.F. (1964)
- Hamilton, D.L., Oxtoby, S. (1986)
- Hammer, J.E., Rutherford, M.J., Hildreth, W. (2002)
- Holtz, F., Behrens, H., Dingwell, D.B., Johannes, W. (1995)
- Holtz, F., Behrens, H., Dingwell, D.B., Taylor, R.P. (1992)
- Holtz, F., Roux, J., Behrens, H., Pichavant, M. (2000)
- Iacono-Marziano, G., Gaillard, F., Pichavant, M. (2008)
- Iacono-Marziano, G., Norizet, Y., Le Trong, E., Gaillard, F. (2012)
- Kennedy, G.C., Wasserburg, G.J., Heard, H.C., Newton, R.C. (1962)
- Khitarov, N.I., Kadik, A.A., Lebedev, Y.B. (1968)
- Khitarov, N.I., Kadik, A.S., Lebedev, E.B. (1963)
- Kogarko, L.N., Burnham, C., Shettle, D. (1977)
- Kohn, S.C., Dupree, R., Smith, M.E. (1989)
- Larsen, J.F., Gardner, J.E. (2004)
- Lesne, P., Scaillet, B., Pichavant, M., Iacono-Marziano, G., Beny, J.-M. (2011)
- Liu, Y., Zhang, Y., Behrens, H. (2005)
- Mangan, M. and Sisson, T. (2000)
- Martel, C., Pichavant, M., Bourdier, J.-L., Traineau, H., Holtz, F., Scaillet, B. (1998)
- McMillan, P., Peral, J., Holloway, J., Coutures, J.-P. (1986)
- Medard, E., Grove, T.L. (2007)
- Métrich, N., Rutherford, M.J. (1998)
- Moore, G., and Carmichael, I.S.E. (1998)
- Moore, G., Roggensack, K., Klonowski, S. (2008)
- Moore, G., Vennemann, T., Carmichael, I.S.E. (1996)
- Moore, G., Vennemann, T., Carmichael, I.S.E. (1998)
- Mysen, B.O., Cody, G.D. (2004)
- Ohlhorst, S., Behrens, H., Holtz, F. (2001)
- Orlova, G.P. (1962)
- Oxtoby, S., Hamilton, D.L. (1976)
- Pallat, O., Elphick, S.C., Brown, W.L. (1992)
- Persikov, E.S. (1974)
- Pineau, F., Shilobreeva, S., Kadik, A., Javoy, M. (1998)
- Roach, A.L. (2005)
- Romano, C., Dingwell, D.B., Behrens, H., Dolfi, D. (1996)
- Schmidt, B.C., Behrens, H. (2008)
- Schmidt, B.C., Holtz, F., Pichavant, M. (1999)
- Shaw, H.R. (1963)
- Shishkina, T.A., Botcharnikov, R.E., Holtz, F., Almeev, R.R., Jazwa, A.M., Jakubiak, A.A. (2014)
- Shishkina, T.A., Botcharnikova, R.E., Holtz, F., Almeev, R.R., Portnyagin, M.V. (2010)
- Silver, L.A., Ihinger, P.D., Stolper, E. (1990)
- Tamic, N., Behrens, H., Holtz, F. (2001)
- Vetere, F., Botcharnikov, R.E., Holtz, F., Behrens, H., de Rosa, R. (2011)
- Vetere, F., Holtz, F., Behrens, H., Botcharnikov, R.E., Fanara, S. (2014)
- Wilke, M., Behrens, H., Burkhard, D.J.M., Rossano, S. (2002)
- Yamashita, S. (1999)
- Yoder Jr., H.S. (1965)

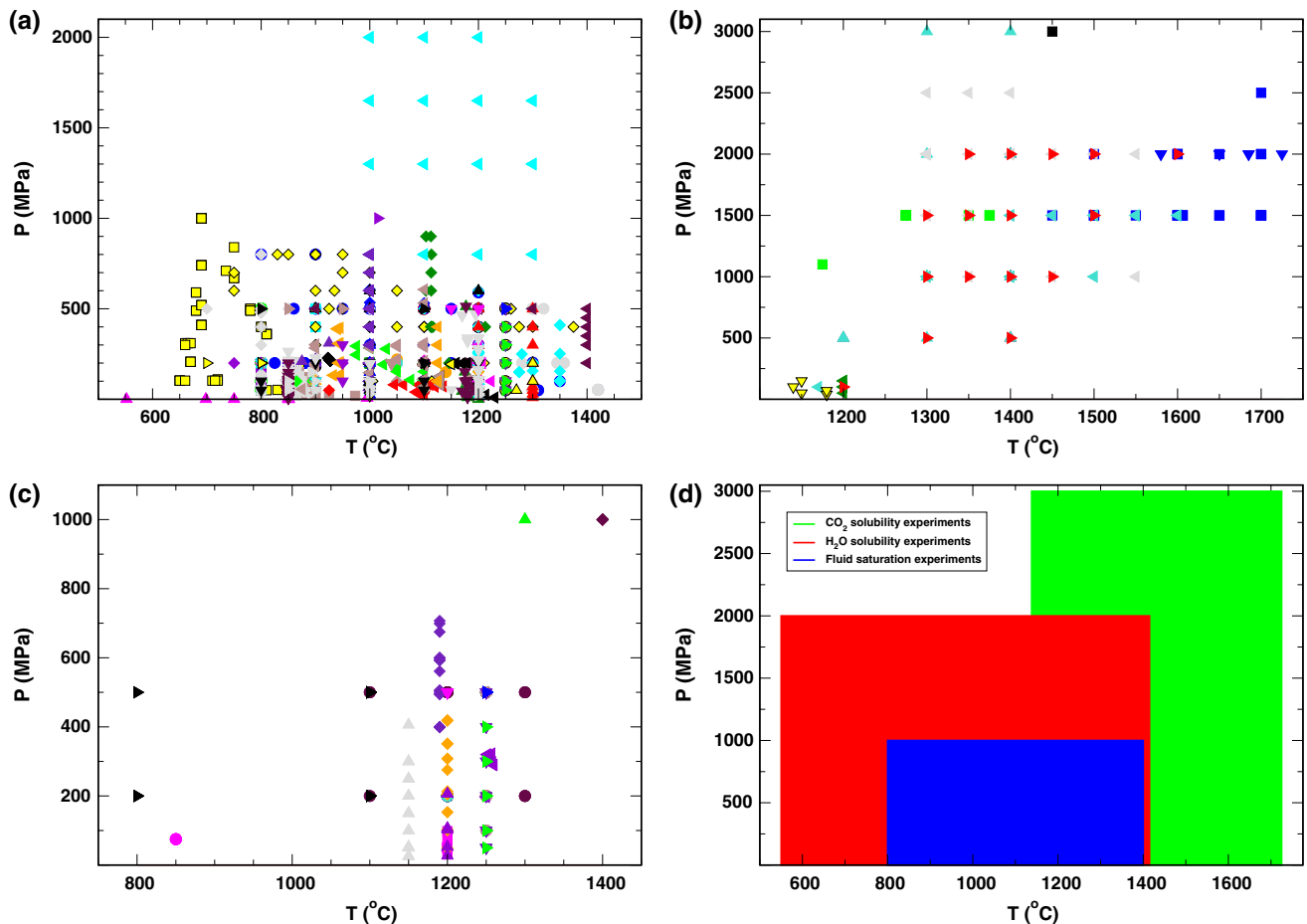


**Fig. 2** Temperature and pressure conditions of calibration data sets. **a** Water solubility experiments, **b** carbon dioxide solubility experiments, **c** saturated mixed  $\text{H}_2\text{O}$ – $\text{CO}_2$  fluid experiments, **d** comparison of coverage of the three data types. *Symbol legend given in Fig. 1*

compared to lower concentrations. The inset graph to the lower right in Fig. 4b illustrates this dependence for the case of a uniform residual error of  $\pm 3$  kJ/mol; it is apparent that this constant residual error generates insignificant errors in predicted water contents at low water concentrations, but quite significant errors at elevated concentrations.

The results plotted in Fig. 4a demonstrate that the MELTS water solubility model is incapable of recovering experimental data on the alkali–silica join (Mysen and Cody 2004) and albite bulk composition at dissolved water contents in excess of 8 wt%. For natural compositions, recovery of water contents is within the expected error envelope at concentrations up to 10 wt%, but systematically offset at higher concentrations Fig. 4b), and recovery fails completely for the peraluminous granitic composition of Burnham and Jahns (1962; see inset upper left in Fig. 4b). The compositional dependence of the systematic offsets is better visualized in Fig. 5, where we have divided the data plotted in Fig. 4b into compositional sectors of the TAS diagram (q.v. Fig. 1a). Figure 5a–c shows that recovery of

water contents is quite good for basaltic through rhyolitic bulk compositions, but systematically offset for alkali-rich mafic compositions (Fig. 5d, e), especially at lower silica contents (Fig. 5d).

We conclude from this assessment of the MELTS water solubility model that, while it is adequate for low-alkali, natural compositions at water contents below 6 wt% (and therefore, lower pressures,  $\sim 300$  MPa), a recalibration of the model against the newer and much expanded data set might improve data recovery. The way to perform this task and maintain internal consistency is to recalibrate MELTS (or rhyolite-MELTS) against the new water solubility database and other more recent experimental solid–liquid experimental data. This exercise is beyond the scope of this paper. Instead, we will use the water solubility data set and recalibrate those parameters in the MELTS liquid thermodynamic model that pertain to the energetic properties of the  $\text{H}_2\text{O}$  component. Pertinent model parameters are listed in Table 2. To perform the recalibration, we abandon the EOS of Nicholls (1980) and adopt that of Ochs and Lange (1997), as discussed above (e.g., Eq. 2).



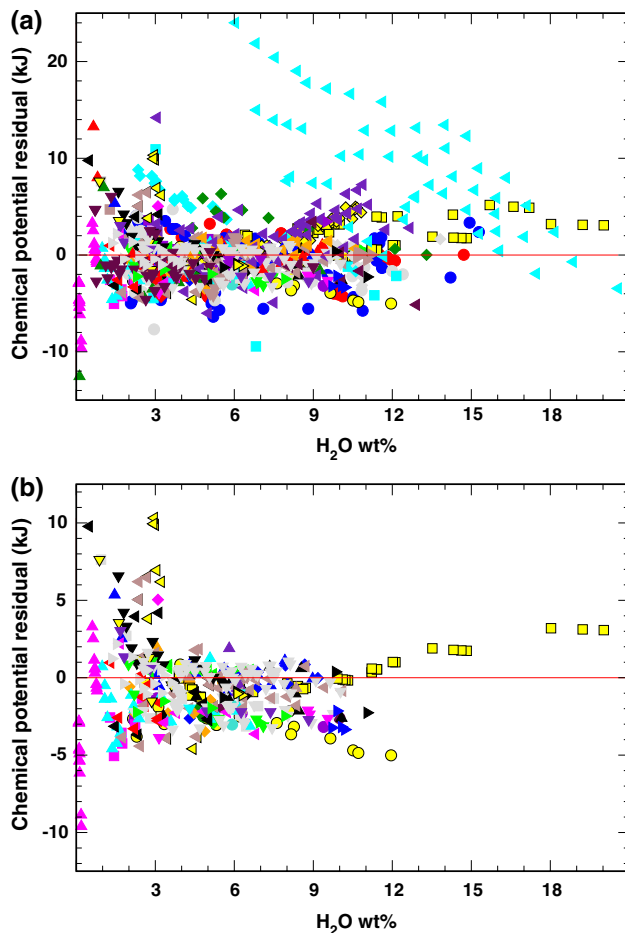


**Fig. 3** Original MELTS model residuals in the chemical potential of  $\text{H}_2\text{O}$  for water solubility experiments plotted as a function of melt water content. *Symbol legend given in Fig. 1a. a* All data from Table 1, *b* natural composition (see text for definition) data from Table 1

Our method of parameter optimization is developed in the ESM Appendix and is based upon singular-value analysis (SVA). This technique permits values (and uncertainties, e.g., Press et al. 1999, p. 698) of all operative parameters to be obtained even if the calibration data set is insufficient to constrain each value uniquely. In brief, the technique remaps the variance of model residuals into linear combinations of model parameters and identifies which linear combinations contribute significantly to the solution. The number of these statistically significant linear combinations of parameters is called the rank of the optimization problem and effectively provides a measure of the number of uncorrelated parameters. Values of all the model parameters are then generated from this smaller uncorrelated subset of linear combinations to obtain the final solution. See Press et al. (1999) or Lawson and Hanson (1974) for a full discussion of the method.

In addition to employing SVA, we have weighted residuals, so that more importance is given to a residual

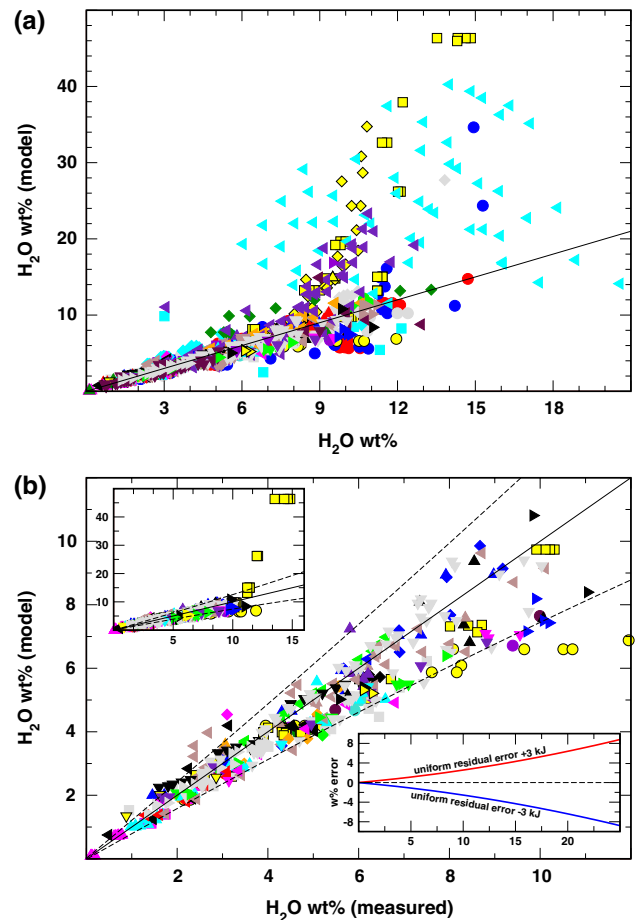


**Fig. 4** Original MELTS model melt water contents (computed by finding a water content that zeroes model residuals) plotted as a function of the measured quantity for water solubility experiments. The *black line* references perfect agreement. *Symbol legend given in Fig. 1a. a* All data from Table 1, *b* natural composition data from Table 1. In (b), the *upper inset* shows all the natural data, while the main body of the figure focuses on water contents below 10 wt%. The *dashed curves* define a data envelope corresponding to a uniform energetic error in residuals of  $\pm 3$  kJ/mol; this function is plotted in the *lower right inset* and discussed in the text

associated with an experiment with high total water content than one with low total water content. This weighting technique permits a higher degree of fidelity in recovering experimental water contents and is motivated by the discussion presented above concerning Fig. 4. The function used to affect the weighting of residuals is the one plotted in the lower right inset of Fig. 4b.<sup>3</sup>

In ESM-Fig. 1 (see Electronic Supplementary Material), we plot an SVA summary analysis of the water model parameter optimization problem. Values for twelve

<sup>3</sup> An empirical polynomial is fitted to the plotted function and yields the equation:  $\text{weight} = 0.0064788 (\text{wt\% H}_2\text{O}) (\text{wt\% H}_2\text{O}) + 0.18906661 (\text{wt\% H}_2\text{O}) + 0.01583988$ .

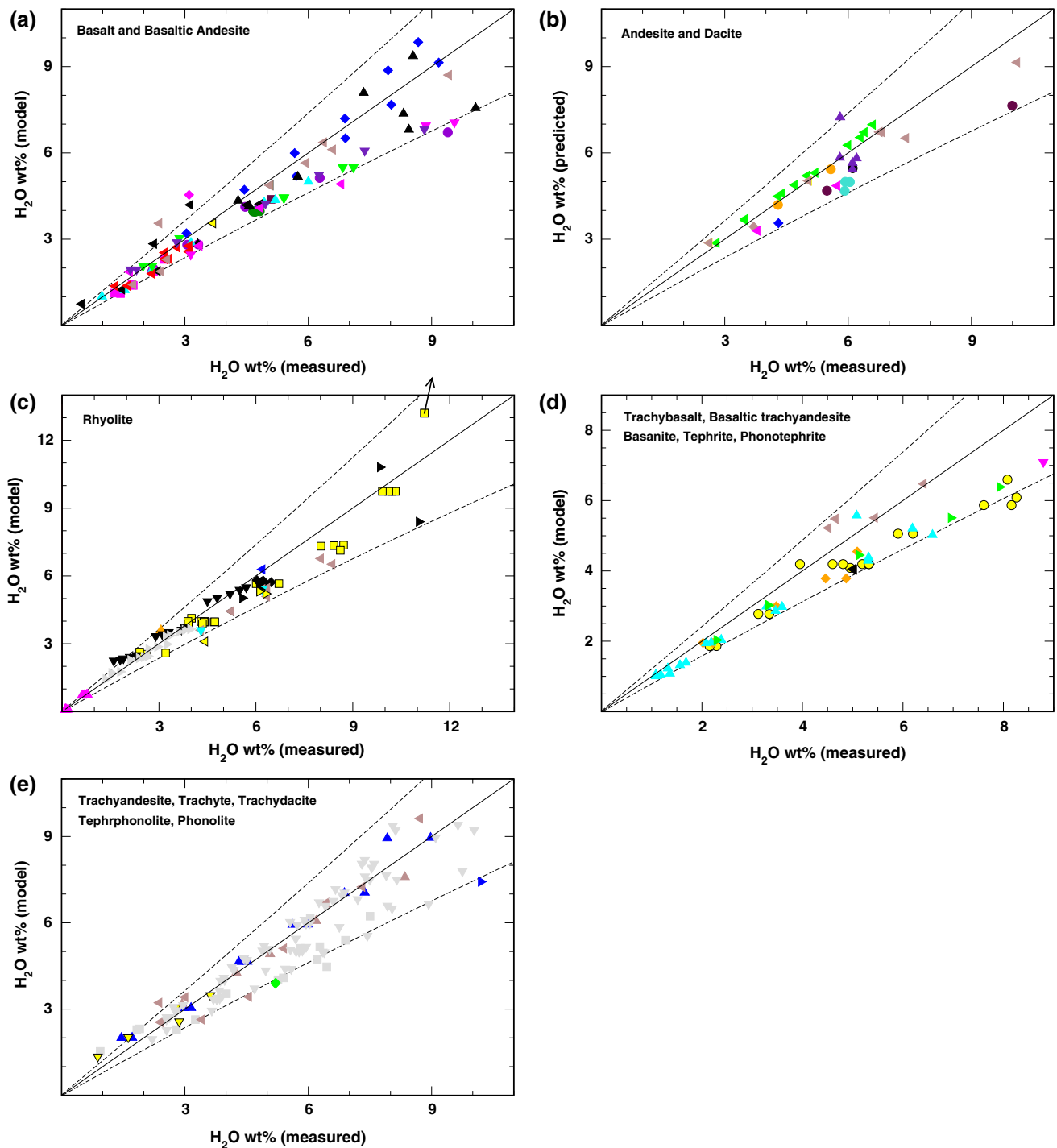


**Fig. 5** Original MELTS model melt water contents plotted as a function of the measured quantity for water solubility experiments. The black line references perfect agreement. Symbol legend given in Fig. 1a. The dashed curves define a data envelope corresponding to a

uniform energetic error in residuals of  $\pm 3$  kJ/mol. Data on bulk compositions: **a** basalts and basaltic andesites, **b** andesites and dacites, **c** rhyolites, **d** alkalic basaltic rocks, **e** trachytic and phonolitic rocks

parameters are extracted (Table 2) from 10 statistically significant linear combinations. Cutoff is chosen at 1 % of the total variance, and the percent variance accounted by each linear combination is plotted along with the contribution

of each model parameter to each linear combination. It is apparent from the figure that the most statistically significant model parameters are the standard-state enthalpy and entropy of the water component in the melt, as well as

**Table 2** Model parameters

Parameter	* = H <sub>2</sub> O	* = CO <sub>2</sub>	* = CaCO <sub>3</sub>	Units (* /mol)
W(SiO <sub>2</sub> , *)	27.557 ± 0.018	–	63.281 ± 1.592	kJ
W(TiO <sub>2</sub> , *)	88.199 ± 2.531	–19.266 ± 0.259	–79.203 ± 0.364	kJ
W(Al <sub>2</sub> O <sub>3</sub> , *)	11.768 ± 2.566	–	46.716 ± 1.176	kJ
W(Fe <sub>2</sub> O <sub>3</sub> , *)	50.105 ± 8.509	–3.187 ± 0.137	65.509 ± 0.171	kJ
W(Fe <sub>2</sub> SiO <sub>4</sub> , *)	30.936 ± 5.818	–32.465 ± 0.308	–72.997 ± 0.290	kJ
W(Mg <sub>2</sub> SiO <sub>4</sub> , *)	20.910 ± 4.486	–40.854 ± 0.641	–24.873 ± 1.037	kJ
W(CaSiO <sub>3</sub> , *)	9.715 ± 2.674	30.012 ± 1.437	37.534 ± 1.012	kJ
W(Na <sub>2</sub> SiO <sub>3</sub> , *)	–82.460 ± 2.423	–	–311.011 ± 0.737	kJ
W(KAlSiO <sub>4</sub> , *)	1.057 ± 1.186	–	–27.865 ± 2.287	kJ
W(Ca <sub>3</sub> (PO <sub>4</sub> ) <sub>2</sub> , *)	44.133 ± 0.336	–3.473 ± 0.030	2.012 ± 0.050	kJ
W(H <sub>2</sub> O, *)		23.255 ± 1.345	7.873 ± 1.449	kJ
$\Delta \hat{H}_{f,*}^o$	2.784 ± 0.235 <sup>a</sup>	–0.631 ± 0.887 <sup>b</sup>	–17.574 ± 0.404	kJ
$\hat{S}_*^o$	2.384 ± 0.214 <sup>a</sup>	–109.393 ± 0.684 <sup>b</sup>	–	J/K
$\hat{V}_*^o$	2.775 <sup>c</sup>	4.0158 ± 0.0206	–1.9034 ± 0.0462	J/bar
$\frac{\partial \hat{V}_*^o}{\partial T}$	1.086 <sup>c</sup>	1.213 <sup>d</sup>	<sup>e</sup>	J/K-bar × 10 <sup>3</sup>
$\frac{\partial \hat{V}_*^o}{\partial P}$	–0.382 <sup>c</sup>	–0.427 <sup>d</sup>	<sup>f</sup>	J/bar <sup>2</sup> × 10 <sup>4</sup>

Interaction parameters for additional liquid components adopted from Ghiorso and Sack (1995). Uncertainties are ± one standard error

<sup>a</sup> Value reported is a correction to that adopted by Ghiorso and Sack (1995) and used in MELTS/rhyolite-MELTS. Ghiorso and Sack (1995) compute enthalpy and entropy from adopted values of –279,992 J/mol and 152.59 J/K-mol, respectively, by adding to these values the *difference* between those computed at one bar and specified temperature from the Haar equation (Haar et al. 1984) and the expressions derived by Robie et al. (1978). The reason for this somewhat Byzantine recipe is discussed in Ghiorso and Sack (1995, p. 210)

<sup>b</sup> Value reported is a correction from quantities calculated at specified temperature and 1 bar from the pure CO<sub>2</sub> fluid model of Duan and Zhang (2006). Adopting this scheme insures that the heat capacity of the melt CO<sub>2</sub> component has a value and temperature dependence consistent with that adopted for the fluid phase. These values consequently identify the difference in enthalpy and entropy between the dissolved CO<sub>2</sub> component in the melt and that of the fluid phase at 1 bar

<sup>c</sup> Adopted value from Ochs and Lange (1997)

<sup>d</sup> Assumed value, see text

<sup>e</sup> Assumed to be identical to  $\frac{\partial \hat{V}_{\text{CO}_2}^o}{\partial T} + \frac{\partial \hat{V}_{\text{CaO}}^o}{\partial T}$ , the latter adopted from Lange and Carmichael (1987)

<sup>f</sup> Assumed to be identical to  $\frac{\partial \hat{V}_{\text{CO}_2}^o}{\partial P} + \frac{\partial \hat{V}_{\text{CaO}}^o}{\partial P}$ , the latter adopted from Kress and Carmichael (1991)

interaction parameters between H<sub>2</sub>O and silica, the alkalis, and alumina. All other model parameters contribute to reducing the variance below the 2 % level.

Only natural composition liquids were used in the recalibration exercise.

Assessment of the recalibrated MELTS water model is provided in Figs. 6 and 7. Figure 6a shows that energetic residuals are randomly distributed about zero and that—by design of the weighting function—these residuals are better recovered at high water contents than low. The distribution of residuals can be compared directly to Fig. 3b demonstrating visually that the recalibration has significantly improved data recovery. In Fig. 6b, the energetic residuals are translated into water contents, which are in turn plotted against those measured. Compare Figs. 6b to 4b to see that the recalibration has improved recovery at intermediate water contents (4–7 wt%) and especially so at higher water contents (>8 wt%). In Fig. 7, the water content

recovery is dissected by rock type. Comparing Figs. 7a–c to 5a–c reveals that recovery of water contents for basalts through rhyolites is somewhat improved by the new calibration, whereas recovery for more alkalic bulk compositions (Fig. 7d, e, compare Fig. 5d, e) is notably better. On the whole, recalibration generates a model that is much improved over that in MELTS or rhyolite-MELTS.

As non-natural bulk compositions were not utilized in the recalibration, it is of interest to examine extrapolated model recovery of these data. In Fig. 8, we plot predicted water contents versus measured for albite liquid (Fig. 8a) and all other non-naturals (Fig. 8b). Recovery for albite liquid is poor for the low-temperature studies of Burnham and Jahns (1962) and for the data of Hamilton and Oxtoby (1986) and Oxtoby and Hamilton (1978) at water contents greater than 8 wt%. Recovery of data on water solubility in SiO<sub>2</sub>–Na<sub>2</sub>O binary melts is poor (Fig. 8b), as in the original model (Fig. 4a). The poor recovery at low temperatures

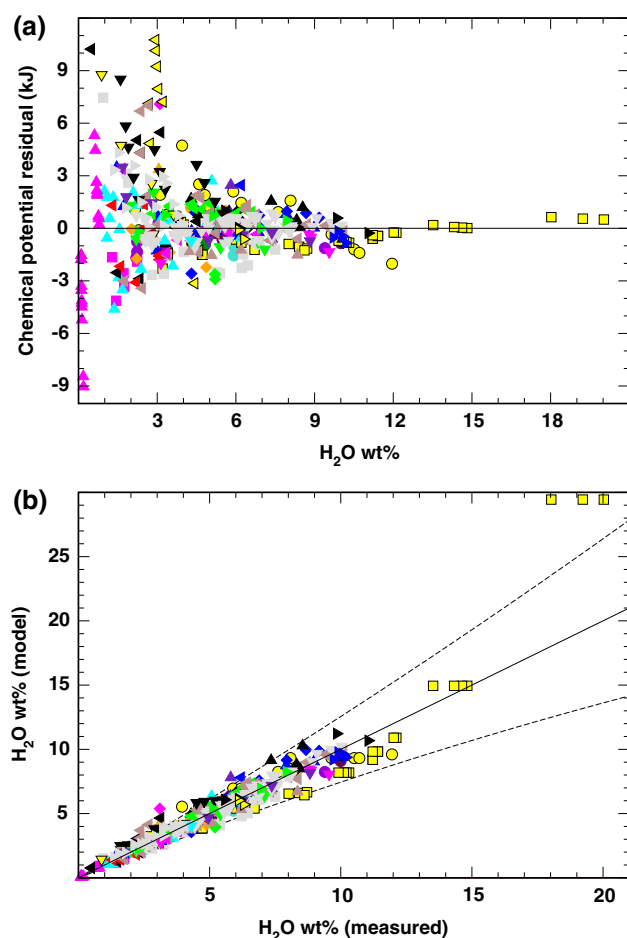


**Fig. 6** Revised MELTS water model. **a** Residuals in the chemical potential of  $\text{H}_2\text{O}$  for natural composition water solubility experiments plotted as a function of melt water content, **b** model melt water contents plotted as a function of the measured quantity for water solubility experiments. In (**b**), the *black line* references perfect agreement, and the *dashed curves* define a data envelope corresponding to a uniform energetic error in residuals of  $\pm 3$  kJ/mol. *Symbol legend* given in Fig. 1a

for the Burnham and Jahns (1962) data set is suggestive. It raises the possibility that the misfit may be due to speciation of dissolved water into both hydroxyl and molecular species, the latter of which is likely more abundant in situ at low temperatures (Nowak and Behrens 1995). While we (and others, e.g., Papale et al. 2006; Moore and Carmichael 1998; Duan 2014) have found no suggestion of the necessity of including water speciation in solubility models for natural compositions, it is nevertheless well known that hydroxyl and molecular species of dissolved water are identified in quenched glass products of water solubility experiments, and that their abundances are systematically related to both temperature and pressure. This issue of speciation can be explored further by focusing solely on the albite melt solubility data and performing two optimized model

fits: (1) a speciation model, constructed on the assumption of ideal mixing of  $\text{NaAlSi}_3\text{O}_8$  liquid and both hydroxyl and molecular water species, and (2) a Burnham model, constructed on the assumption of ideal mixing of hydroxyl species and  $\text{NaAlSi}_3\text{O}_8$  liquid. For the speciation model, thermodynamic properties of water in both structural configurations are extracted from the fit, and the entropy of the hydroxyl species is taken as the square of the mole fraction (Eq. 1, and the Burnham model). Results of this modeling exercise are plotted in Fig. 9, with model parameters listed in the figure legend. Several interesting features are apparent. First, it is clear that by isolating the albite data, it is possible to construct a representative model using either the speciation or Burnham formulation, and that the data sets of Oxtoby and Hamilton (1978) and Hamilton and Oxtoby (1986) are outliers in either case. Second, the temperature dependence of hydroxyl molecular water speciation, extracted here solely from the solubility relations, is consistent with measured trends inferred from NIR spectra (e.g., Stolper 1989; Nowak and Behrens 1995). Third, the pressure dependence of speciation (even when the effect of varying temperature is subtracted) differs from that suggested by Silver and Stolper (1989) and Hui et al. (2008). The pressure effect extracted by the model is to stabilize the hydroxyl species with elevated pressure, while the trends exhibited from speciation measurements on glasses quenched from high-pressure experiments suggest negligible pressure stabilization below 1 GPa; the inference here is that the molecular species has a smaller molar volume than two hydroxyl units. The important conclusion to draw from modeling the  $\text{NaAlSi}_3\text{O}_8$  liquid water solubility data is that either the speciation or the Burnham model can recover the solubility array. Therefore, inclusion of speciation in the thermodynamic formulation is unnecessary if the objective is to recover the solubility relations. We infer from this observation that the inability of the recalibrated MELTS water model to recover the low-temperature data of Burnham and Jahns (1962) is not a consequence of ignoring water speciation, but rather a manifestation that the MELTS anhydrous thermodynamic model is incapable of characterizing the enthalpy of pure albite liquid, probably because the excess enthalpy terms in the model, which are derived by fitting phase equilibria in multicomponent systems, cannot extrapolate accurately to  $\text{NaAlSi}_3\text{O}_8$  bulk composition. The fact that the problem manifests at low temperature corroborates this conclusion in that entropy of mixing tends to dominate melt energetics at elevated temperature.

The quality of the data recovery of the natural composition experiments shown in Fig. 8 justifies the use of the reformulated MELTS water solubility model as a basis for the mixed fluid saturation model proposed below. The formulation and calibration of that model is developed in the next section.

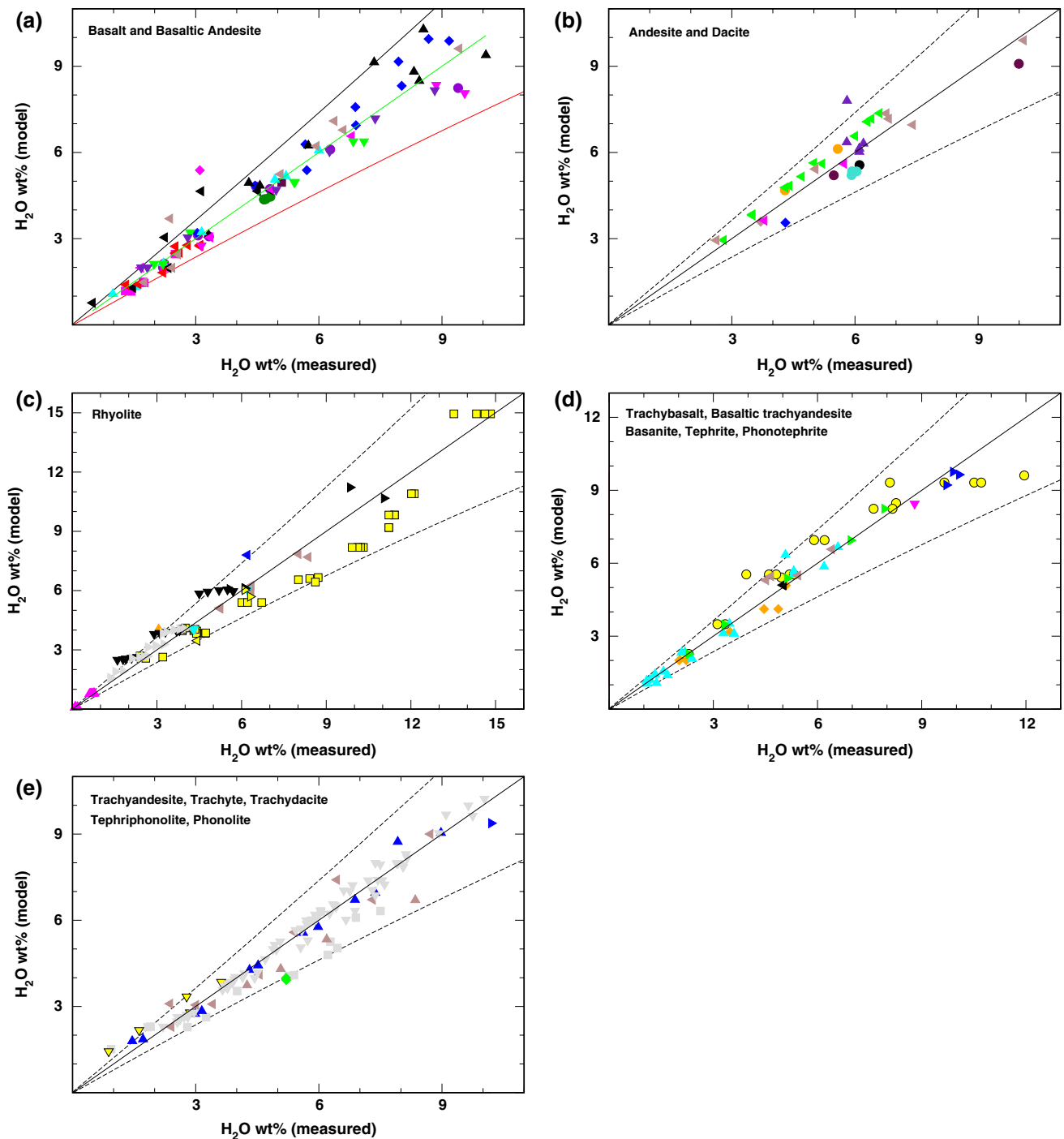


**Fig. 7** Revised MELTS model melt water contents plotted as a function of the measured quantity for water solubility experiments. The black line references perfect agreement. Symbol legend given in Fig. 1a. The dashed curves define a data envelope corresponding to a

uniform energetic error in residuals of  $\pm 3$  kJ/mol. Data on bulk compositions: **a** basalts and basaltic andesites, **b** andesites and dacites, **c** rhyolites, **d** alkalic basaltic rocks, **e** trachytic and phonolitic rocks

### Carbon dioxide solubility in silicate liquids

In addition to adopting the model of Duan and Zhang (2006) for thermodynamic properties of the fluid phase, in order to extend our recalibrated water solubility model to

include mixed fluids, a choice must be made for specifying the configurational entropy of dissolved carbon dioxide in the melt. Fine and Stolper (1985, 1986 and thereafter many others: see the excellent summary in Guillot and Sator 2011) suggest, from FTIR studies of quenched glass

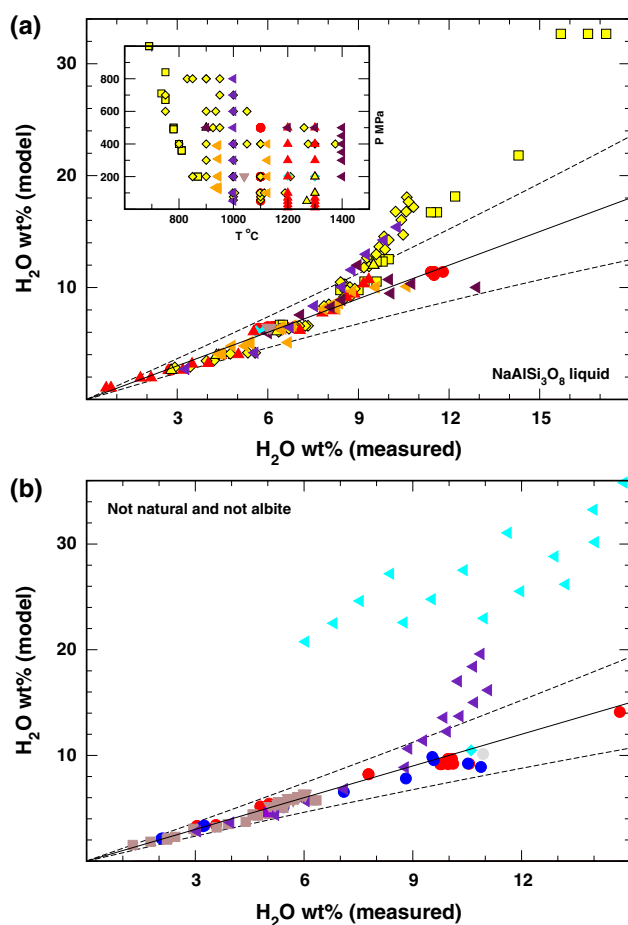


**Fig. 8** Revised MELTS model melt water contents plotted as a function of the measured quantity for non-natural composition liquids. **a** NaAlSi<sub>3</sub>O<sub>8</sub> (albite) bulk composition melts, **b** all other non-natural composition melts. The black line references perfect agreement. Symbol legend given in Fig. 1a. The dashed curves define a data envelope corresponding to a uniform energetic error in residuals of  $\pm 3$  kJ/mol

experimental run products, that carbon dioxide exists in the melt as two distinct species: molecular CO<sub>2</sub> and carbonate ions, the latter presumably associated principally with alkali metal and alkali earth cations. Theirs and subsequent studies also infer the predominance of molecular CO<sub>2</sub> in rhyolitic and more siliceous compositions with increasing importance of carbonate at decreasing SiO<sub>2</sub> concentration. Unlike the situation with dissolved water in silicate melts, where the mechanism of diffusion is a first-order function of speciation (Wasserburg 1988; Behrens and Nowak 1997; recent literature summary in Zhang and Ni 2010), the diffusivity of carbon dioxide does not exhibit a strong dependence on the relative abundance of molecular CO<sub>2</sub> and carbonate species (Nowak et al. 2004). This observation suggests that it may be possible to model carbon dioxide solubility in silicate liquids with a single melt species. Indeed, that assumption has proved successful in

previous models of CO<sub>2</sub> solubility in silicate liquids (Spera and Bergman 1980; Papale 1997, 1999; Papale et al. 2006; Duan 2014), although alternate formulations that embody speciation (e.g., Dixon et al. 1995; Newman and Lowenstein 2002) are equally effective. The recent molecular dynamics study of Guillot and Sator (2011) has explored molecular and carbonate speciation as a function of  $T$ ,  $P$ , and composition. They find that increasing temperature stabilizes the carbonate species as does pressure, but that in simulations for kimberlitic, basaltic, and rhyolitic composition liquids below 2 GPa (all at a temperature of 2000 K), molecular CO<sub>2</sub> is the predominant melt species—essentially controlling the solubility of dissolved carbon dioxide.

Despite the attractive simplicity of formulating a thermodynamic model with a single component of carbon, in order to examine the consequences of carbonate speciation on solubility relations, we construct an associated regular solution model that contains both molecular and carbonate species. Specifically, we assume that the lack of significant carbonate in rhyolitic glass implies that alkali–metal carbonate complexes are less important carbonate reservoirs than those of the alkali earths. Consequently, the model we propose that extends the hydrous liquid model of MELTS contains two carbon species, CO<sub>2</sub> and CaCO<sub>3</sub>. Details of model formulation, including expressions for the Gibbs free energy, methods of calculating a homogeneous equilibrium distribution of melt carbon species, and expressions for the chemical potentials of melt components, are provided in the ESM Appendix. We will evaluate this model against the carbon dioxide solubility and mixed fluid saturation databases, with an eye toward establishing the necessity of including the CaCO<sub>3</sub> species and the possible need of adding additional carbonate species of the alkali metals and alkali earths. Carbon-related parameters of the melt model are listed in Table 2.

The model requires an expression for the standard-state chemical potential of the CO<sub>2</sub> component in the melt (ESM Appendix, Eq. 27), which is not the same as the endmember component in the fluid phase, whose properties we compute from Duan and Zhang (2006; ESM Appendix, Eq. 8). For the melt,  $\mu_{\text{CO}_2}^0$  is parameterized as:

$$\mu_{\text{CO}_2}^0 = \bar{h}_{\text{CO}_2}^0 - T\bar{s}_{\text{CO}_2}^0 + \left[ \bar{v}_{\text{CO}_2}^0 + \frac{\partial \bar{v}_{\text{CO}_2}^0}{\partial T}(T - 1400) + \frac{1}{2} \frac{\partial \bar{v}_{\text{CO}_2}^0}{\partial P}(P - 1) \right] (P - 1) \quad (3)$$

where  $\bar{h}_{\text{CO}_2}^0$  is the partial molar enthalpy of the pure component,  $\bar{s}_{\text{CO}_2}^0$  is the partial molar entropy, and  $\bar{v}_{\text{CO}_2}^0$  is the partial molar volume. In (Eq. 3), the units of temperature and pressure are assumed as K and bars. None of these three standard-state parameters have been measured, but there are a number of previous estimates for  $\bar{v}_{\text{CO}_2}^0$ .



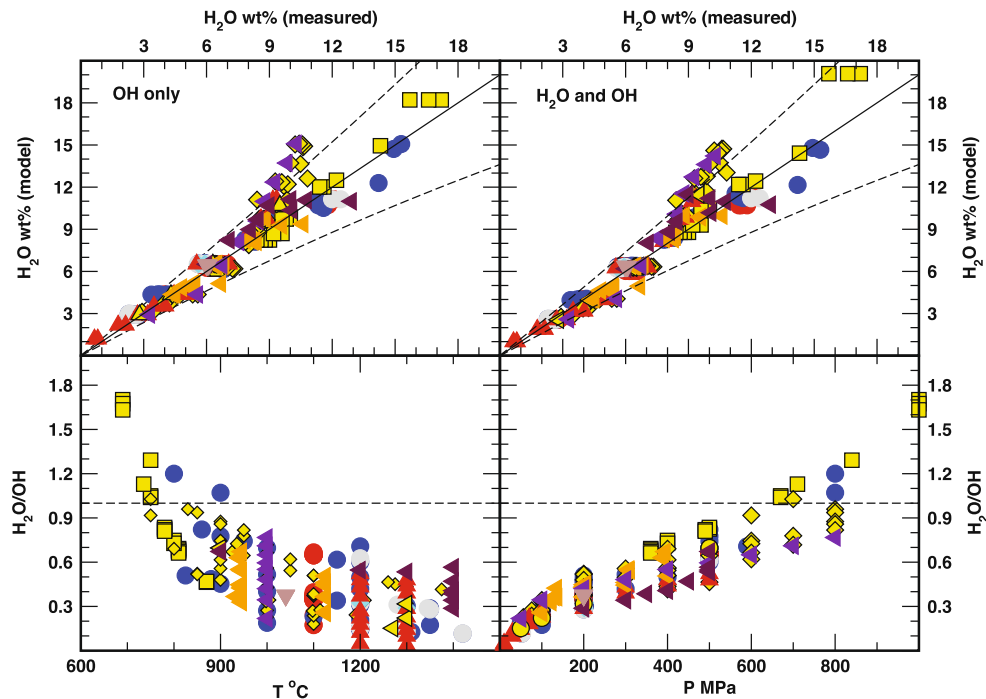


**Fig. 9** Model water contents plotted versus measured quantities for experiments on  $\text{NaAlSi}_3\text{O}_8$  composition liquids computed from models calibrated specifically for this bulk composition: (upper left panel) ideal solution model constructed on the assumption that water dissolves as an hydroxyl melt species (upper right panel) ideal associated solution model constructed on the assumption that water dissolves as both molecular and hydroxyl melt species (lower left panel) ratio of molecular to hydroxyl species computed for the associated solution model plotted as a function of temperature (lower right panel) same ratio, plotted as a function of pressure. In the top two panels, the black line references perfect agreement, and the dashed curves define a data envelope corresponding to a uniform ener-

getic error in residuals of  $\pm 3$  kJ/mol. In the bottom two panels, the dashed line references a ratio of unity. Symbol legend given in Fig. 1a. Parameters for the hydroxyl-only model:  $\Delta \hat{H}_{\text{f,H}_2\text{O}}^\circ = 14.154$  kJ/mol,  $\hat{S}_{\text{H}_2\text{O}}^\circ = 6.162$  J/K-mol,  $\hat{V}_{\text{H}_2\text{O}}^\circ = 2.359$  J/bar-mol. Parameters for the hydroxyl, molecular speciation model:  $\Delta \hat{H}_{\text{f,H}_2\text{O as 2OH}^-}^\circ = 16.482$  kJ/mol,  $\hat{S}_{\text{H}_2\text{O as 2OH}^-}^\circ = 4.134$  J/K-mol,  $\hat{V}_{\text{H}_2\text{O as 2OH}^-}^\circ = 3.545$  J/bar-mol,  $\Delta \hat{H}_{\text{f,H}_2\text{O as H}_2\text{O}}^\circ - \Delta \hat{H}_{\text{f,H}_2\text{O as 2OH}^-}^\circ = -15.434$  kJ/mol,  $\hat{S}_{\text{H}_2\text{O as H}_2\text{O}}^\circ - \hat{S}_{\text{H}_2\text{O as 2OH}^-}^\circ = -6.971$  J/K-mol,  $\hat{V}_{\text{H}_2\text{O as H}_2\text{O}}^\circ - \hat{V}_{\text{H}_2\text{O as 2OH}^-}^\circ = -0.814$  J/bar-mol. The volumetric quantities are referenced to 1400 °C

Spera and Bergman (1980) estimated  $\bar{v}_{\text{CO}_2}^\circ$  by analyzing experimental data on  $\text{CO}_2$  solubility from the literature and obtained a value of 34.9 cc/mol (at 1460 °C) to 33.5 cc/mol (at 1620 °C) for  $\text{NaAlSi}_3\text{O}_8$  liquid, 34.1–32.7 cc/mol for  $\text{NaAlSi}_2\text{O}_6$  liquid, 34.5–30.7 cc/mol for  $\text{NaAlSiO}_4$  liquid, 33.9 cc/mol for molten andesite, 32.7 cc/mol for molten tholeiite, and 29.3 cc/mol for liquids of olivine melilite composition. They suggest that a common value of ~30 cc/mol can be universally applied, that this value is independent of  $T$  and  $P$ , and that there is no marked compositional dependence to  $\bar{v}_{\text{CO}_2}^\circ$ . In agreement with Spera and Bergman (1980), Stolper and Holloway (1988) obtain a value of 33 cc/mol for basaltic composition liquid at 1200 °C from solubility experiments at low  $P$ . Lange (1994) summarizes values of  $\bar{v}_{\text{CO}_2}^\circ$  from studies that determine relative abundances of molecular  $\text{CO}_2$  and carbonate and suggests that the best estimates fall in the range 21–28 cc/mol, the smaller being applicable to carbonate-dominated systems. Newman and Lowenstern (2002) adopt a value of 28 cc/mol

for rhyolite liquid and 23 cc/mol for basaltic liquid in their solubility models. Liu and Lange (2003) have analyzed fusion curves of molten carbonate liquids and estimated  $\bar{v}_{\text{CO}_2}^\circ$  at 1100 K as 25.8 cc/mol (molten  $\text{CaCO}_3$ ), 27.7 cc/mol (molten  $\text{Li}_2\text{CO}_3$ ), 28.7 cc/mol (molten  $\text{Na}_2\text{CO}_3$ ), and 32.4 cc/mol (molten  $\text{K}_2\text{CO}_3$ ). They suggest that the most applicable value for natural melts is close to the number for molten  $\text{CaCO}_3$ . Recently, Duncan and Agee (2011) determined, using the sink–float experimental method, a value for  $\bar{v}_{\text{CO}_2}^\circ$  for molten peridotite at 2123 K in the pressure range 4.3–5.5 GPa to be 23.71 cc/mol to 22.06 cc/mol, respectively, which yields their model estimate for  $\bar{v}_{\text{CO}_2}^\circ$  at 1 bar as 36.57 cc/mol. Guillot and Sator (2011) compute from first principles a value of ~25.5 cc/mol for kimberlitic liquid and ~30.5 cc/mol for MORB liquid (both at 2000 K).

Estimates of  $\bar{v}_{\text{CO}_2}^\circ$  are obviously varied, and some of this variation may be due to the temperature dependence of the molar volume:  $\partial \bar{v}_{\text{CO}_2}^\circ / \partial T$ . The only estimate of this quantity comes from Liu and Lange (2003,  $3.41 \pm 2.23 \times 10^{-3}$  cc/mol-K),

but their value is derived from the analysis of the fusion curve of  $\text{CaCO}_3$ .

Papale et al. (2006) used an equation of the form of (4) in their analysis of  $\text{CO}_2$  solubility data. They find values of  $\bar{v}_{\text{CO}_2}^0$ ,  $\partial\bar{v}_{\text{CO}_2}^0/\partial T$ , and  $\partial\bar{v}_{\text{CO}_2}^0/\partial P$  of 24.92 cc/mol,  $13.44 \times 10^{-3}$  cc/mol-K, and  $2.107 \times 10^{-9}$  cc/mol-bar. Their  $\partial\bar{v}_{\text{CO}_2}^0/\partial T$  is much larger than that suggested by Liu and Lange (2003), and their value of  $\partial\bar{v}_{\text{CO}_2}^0/\partial P$  is clearly of the wrong sign as it implies a negative compressibility or bulk modulus; that implausible value of  $\partial\bar{v}_{\text{CO}_2}^0/\partial P$  may be ascribed in part to the fact that Papale et al. (2006) made the melt interaction parameters involving the  $\text{CO}_2$  component ( $W_{i,\text{CO}_2}$ ) pressure-dependent; consequently, in practical application their modeled value of  $\partial\bar{v}_{\text{CO}_2}^0/\partial P$  of  $\text{CO}_2$  in a mixed melt could still be thermodynamically consistent, i.e., negative. Duan (2014) extracts a standard-state molar volume of  $25.03 + 1973.44 \times 10^{-3} P/T - 1.06 \times 10^{-3} P$  from their analysis of  $\text{CO}_2$  solubility and mixed fluid saturation data, from which  $\partial\bar{v}_{\text{CO}_2}^0/\partial T$  and  $\partial\bar{v}_{\text{CO}_2}^0/\partial P$  at 1400 °C and 1 bar are  $-7.05 \times 10^{-7}$  cc/mol K and  $1.19 \times 10^{-4}$  cc/mol-bar, respectively. Duan's value of  $\partial\bar{v}_{\text{CO}_2}^0/\partial T$  is implausibly small, and his value for  $\partial\bar{v}_{\text{CO}_2}^0/\partial P$  has the wrong sign. It is interesting that both Papale et al. (2006) and Duan (2014) obtain by parameter regression physically implausible estimates for the compressibility of dissolved  $\text{CO}_2$  in melts. In part, this result must be due to model parameter correlation resulting from deficiencies in the experimental calibration database, but it may also be due to simplistic assumptions regarding  $\text{CO}_2$  melt speciation.

Given the  $T$ - $P$  distribution of available  $\text{CO}_2$  solubility data (Fig. 2b, and mixed fluid saturation data, Fig. 2c) and recognizing that the solubility of  $\text{CO}_2$  in silicate liquid is quite low at lower pressure regardless of composition, we have opted not to extract  $\partial\bar{v}_{\text{CO}_2}^0/\partial T$  or  $\partial\bar{v}_{\text{CO}_2}^0/\partial P$  by parameter regression. We set these quantities to numerical values consistent with Ochs and Lange's (1997) analysis for  $\text{H}_2\text{O}$  (Table 2), scaled by the ratio of molecular weights of  $\text{CO}_2$  and  $\text{H}_2\text{O}$ . We also assume that

$$\frac{\partial\bar{v}_{\text{CaCO}_3}^0}{\partial P} = \frac{\partial\bar{v}_{\text{CO}_2}^0}{\partial P} + \frac{\partial\bar{v}_{\text{CaO}}^0}{\partial P} \quad (4)$$

and

$$\frac{\partial\bar{v}_{\text{CaCO}_3}^0}{\partial T} = \frac{\partial\bar{v}_{\text{CO}_2}^0}{\partial T} + \frac{\partial\bar{v}_{\text{CaO}}^0}{\partial T} \quad (5)$$

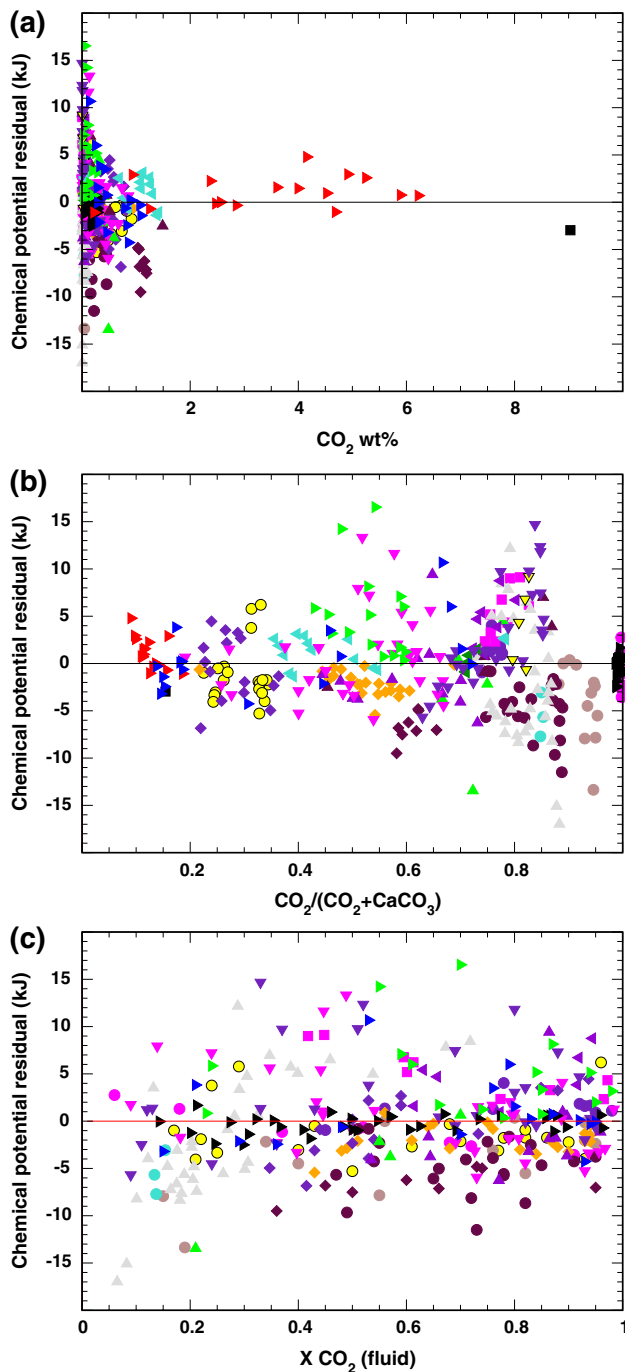
with indicated quantities for the  $\text{CaO}$  melt component taken from Lange and Carmichael (1987). However, we relax the usual ideal mixing assumption that would impose the constraint  $\bar{v}_{\text{CaCO}_3}^0 = \bar{v}_{\text{CO}_2}^0 + \bar{v}_{\text{CaO}}^0$ , and extract both  $\bar{v}_{\text{CO}_2}^0$  and  $\bar{v}_{\text{CaCO}_3}^0$  during model optimization.

Model parameters (Table 2) are obtained by optimization of residuals ( $\Delta\mu_{\text{CO}_2}^{\text{residual}}$ ) against natural compositions from the pure  $\text{CO}_2$  solubility studies and from all the mixed fluid

studies (Table 1). Because speciation of carbon renders the parameter optimization process intrinsically nonlinear, the optimization is carried out in a series of SVA steps (this method is discussed in the ESM Appendix), and an initial guess of parameter values is provided to the optimization procedure that predisposes molecular  $\text{CO}_2$  to be the dominant carbon species at lower  $T$  and in highly silicic compositions. There are 23 model parameters involved in the regression. Results from the SVA of the last phase of the optimization are presented in ESM-Fig. 2 (see Electronic Supplementary Material). More than 90 % of the residual variance is accounted for by the first five uncorrelated linear combinations (ESM-Fig. 2) of model parameters, and these linear combinations are exclusively constructed from standard-state properties. The most important "excess" energy parameters involve  $\text{CO}_2$ - and  $\text{CaCO}_3$ - $\text{H}_2\text{O}$  interactions, which enter into linear combinations 5–8. We chose a cutoff "rank" for this problem of 15, as this cutoff accounts for residual variance greater than 0.1 % and is the point at which extracted values of model parameters change little with inclusion of additional linear combinations. Parameter values and their uncertainties are reported in Table 2.

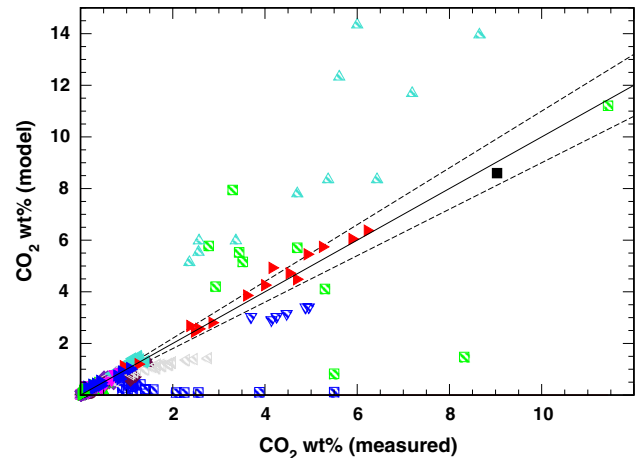
The quality of the model fit is best examined by looking at energetic residuals, predicted  $\text{CO}_2$  melt contents, predicted mixed fluid compositions, and modeled  $\text{H}_2\text{O}$ - $\text{CO}_2$  saturation relations. Energetic residuals are plotted in Fig. 10. The standard error of residuals for the  $\text{CO}_2$  parameter optimization is  $\sim 3$  kJ/mol. The pronounced scattering of residuals at low total dissolved  $\text{CO}_2$  contents (Fig. 10a) is due to the sensitivity of the logarithm to small variations in mole fraction and is to be expected. In Fig. 10b, residuals are plotted as a function of the modeled proportion of molecular  $\text{CO}_2$  species to total dissolved carbon. Although no constraints derived from species abundances in quenched glass from experimental run products were imposed on the model parameterization, the results are qualitatively consistent with those observations. Specifically, rhyolitic and dacitic bulk compositions are dominated by molecular  $\text{CO}_2$ , and proportions of carbonate increase with decreasing silica content. In addition, there is little correlation of energetic residual to alkali content, which supports our assumption that sodium and potassium carbonate complexes are not required to model the data array. The mixed fluid residuals plotted in Fig. 10c show that the model recovers experiments across the entire range of fluid compositions without bias.

Figure 11 casts energetic model residuals into estimates of melt  $\text{CO}_2$  contents. The figure shows that recovery of  $\text{CO}_2$  contents is generally within 10 % of the measured quantity for natural composition liquids. In the same figure, we have also plotted predicted  $\text{CO}_2$  contents from experimental solubility data on bulk compositions that were not used in the calibration because they fall outside the



**Fig. 10** CO<sub>2</sub> model regression: **a** energetic model residuals in the chemical potential of CO<sub>2</sub> for carbon dioxide solubility and mixed fluid saturation experiments plotted as a function of **a** melt CO<sub>2</sub> content, **b** the modeled molar ratio of molecular CO<sub>2</sub> to total dissolved carbon in the melt, and **c** the reported mole fraction of CO<sub>2</sub> in the mixed fluid saturation experiments. *Symbol legend given in Fig. 1b, c*

composition space applicable to the MELTS models. The data from Morizet et al. (2002) are from a synthetic phonolite with high alumina and soda concentrations. The data from Brooker et al. (1999) were obtained on a composition



**Fig. 11** Model melt carbon dioxide contents (computed by finding a CO<sub>2</sub> concentration that zeroes model residuals) plotted as a function of measured melt CO<sub>2</sub> content for CO<sub>2</sub> solubility experiments and mixed fluid saturation experiments. The *black line* references perfect agreement; *dashed lines* denote  $\pm 10\%$ . *Symbol legend given in Fig. 1b, c*. The *hatched symbols* refer to non-natural bulk composition experiments that were not used in model parameter optimization

in the soda–alumina–silica system. The data of Matthey et al. (1990) are on liquids in the system silica–alumina–lime–soda, as are most of the data of Brooker et al. (2001). The best synthetic data recovery is for the calcium–magnesium–silica liquids of Rai et al. (1983). It is clear from the figure that the model for CO<sub>2</sub> solubility developed in this paper does not work well for non-natural liquids that are Na<sub>2</sub>O-bearing but have absent or near-absent concentrations of CaO. This observation suggests that a solubility model for these liquids could be extended from the present model by incorporation of a Na<sub>2</sub>CO<sub>3</sub> melt species. However, in practical terms, if the reader is interested in a CO<sub>2</sub> solubility model that captures these synthetic liquids, they should use the model of Papale et al. (2006) or Duan (2014). Finally, it should also be noted that all of the mixed fluid experiments have natural compositions, and their CO<sub>2</sub> content recovery will be examined in detail below.

For the mixed fluid data set, energetic residuals may be recast into estimates of melt H<sub>2</sub>O and CO<sub>2</sub> contents, or in terms of fluid H<sub>2</sub>O, CO<sub>2</sub> mol fractions, or some combination of the two. Below, we construct predicted H<sub>2</sub>O–CO<sub>2</sub> saturation diagrams for all of the mixed fluid experimental bulk compositions. In Fig. 12, we examine the estimates of fluid composition and compare these to experimentally reported compositions. The mole fractions of H<sub>2</sub>O and CO<sub>2</sub> in the fluid are estimated independently by zeroing the residual in  $\Delta\mu_{\text{H}_2\text{O}}^{\text{residual}}$  and  $\Delta\mu_{\text{CO}_2}^{\text{residual}}$ , respectively, ascribing all residual error to the composition of the fluid phase. In Fig. 12c, the sum of these estimates is plotted against reported fluid composition. The calculated sum should

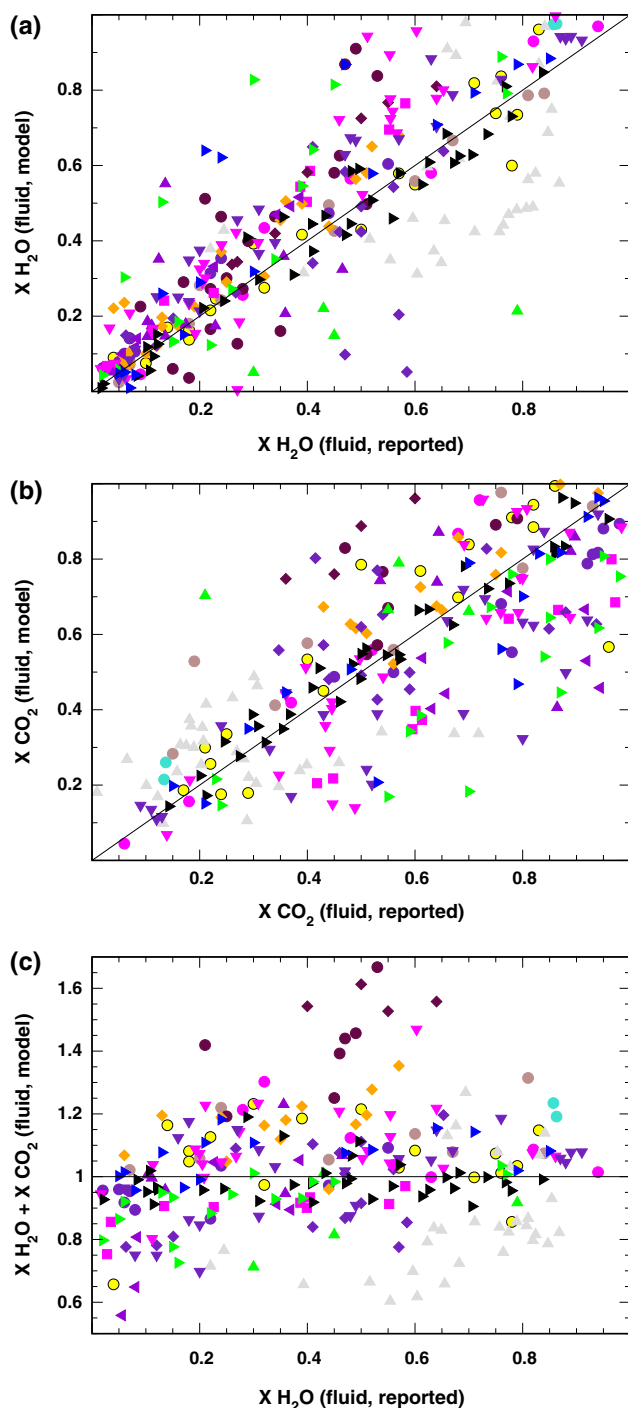


**Fig. 12** Model fluid water and carbon dioxide mole fractions (computed by finding concentrations that zero model residuals) plotted as a function of fluid composition. **a**  $\text{H}_2\text{O}$  fluid mole fraction (computed from  $\text{H}_2\text{O}$  chemical potential residuals) plotted against reported fluid water content, **b**  $\text{CO}_2$  fluid mole fraction (computed from  $\text{CO}_2$  chemical potential residuals) plotted against reported fluid carbon dioxide content, **c** sum of independent model estimates of fluid composition plotted against reported fluid water content. The black line references perfect agreement. Symbol legend given in Fig. 1c

of course be unity, and any deviation from unity reveals model error in recovery of the reported fluid composition. In the majority of the mixed fluid experiments tabulated in Table 1, the fluid composition was estimated and not directly measured. The most commonly used approach is to determine fluid  $\text{H}_2\text{O}$  and  $\text{CO}_2$  contents by mass balance using the weight-loss method (Behrens et al. 2009; Botcharnikov et al. 2005a, b, 2006, 2007; Jakobsson 1997; Lesne et al. 2011a; Shishkina et al. 2010, 2014; Tamic et al. 2001; Vetere et al. 2011, 2014). Other methods include calculation of fluid composition from the total pressure, estimates of  $\text{CO}_2$  fugacity, and an assumed equation of state (Behrens et al. 2004a, b; Iacono-Marziano et al. 2012; Lesne et al. 2011b) and micro-Raman spectroscopy of experimentally produced fluid inclusions (Morizet et al. 2010). The most rigorous and direct method to determine experimental fluid composition (Moore 2008) is vacuum manometry of the fluid-separated run product. Only the studies of Blank et al. (1993), Dixon et al. (1995), and Iacovino et al. (2013) utilize that analytical technique. The estimated fluid compositions of Dixon et al. (1995) and Iacovino et al. (2013) are randomly scattered and within  $\sim 10\%$  of the unity line in Fig. 12c. Recovery of Blank et al.'s (1993) fluid data shows greater scatter at  $X \text{H}_2\text{O} < 0.5$ , but the total concentrations of  $\text{CO}_2$  in their experiments are so low, that a larger recovery error is expected. Other data show systematic bias; on the whole, the error expected from indirect estimates of fluid composition (like the weight-loss method) is typically on the order of 10 %, but it is not unusual to report analytical errors at low fluid  $\text{H}_2\text{O}$  contents of 50–100 % or even higher (Moore 2008). An additional consideration that pertains to systematic bias in either energetic residuals (Fig. 10b, c) or predicted fluid composition (Fig. 12a, b) is that the data of Lesne et al. (2011a) were obtained on bulk compositions that contain additional volatile components (S, Cl), whose energetic consequences we have not considered. Similarly, the data of Botcharnikov et al. (2007) are obtained on Cl-bearing fluids. We should also note that the experimental run conditions of Botcharnikov et al. (2006) and Morizet et al. (2010) are reducing, and the fluid/melt system consequently contains reduced carbon species.

In ESM-Fig. 3 (see Electronic Supplementary Material), saturation state relations are calculated for the experimental compositions and conditions of each mixed fluid calibration data set of Table 1, and these model curves are compared to reported melt volatile concentrations. This analysis is exhaustive of all published mixed fluid saturation state studies in order to give the reader a sense of the successes and failures of the model across a broad spectrum of natural composition liquids. Reported uncertainties are plotted as  $\pm 2\sigma$ . Uncertainty in determination of melt  $\text{H}_2\text{O}$



and CO<sub>2</sub> contents is typically in the range 10–20 % relative when determined using FTIR methods. H<sub>2</sub>O determined by more traditional methods of titration are often more precise if dissolved water concentration is high. Behrens et al. (2004a), for example, report relative errors on H<sub>2</sub>O melt contents between 2 and 20 % determined using titration. An important consideration in evaluating the model-data comparison of ESM-Fig. 3 is the fact that model curves are drawn assuming the reported nominal composition of the melt is invariant. In practice, this is not the case. Iron loss to capsules is commonplace, and alkali loss is a potential problem; often, the compositions of experimental run products vary appreciably from the nominal values. In performing the model fit, actual experimental run product compositions were utilized (if such data were reported or could be obtained from the authors), but in ESM-Fig. 3, plotted experimental measurements may very well reflect volatile content determinations for experimental liquids that differ from the nominal model curves. Another complication (which is also the case for water solubility data) is that at higher pressures, there is likely appreciable dissolution of “anhydrous” melt components into the fluid phase, which would both alter the nominal bulk composition of the silicate melt and affect the thermodynamic properties of the fluid. This elemental partitioning has not been measured for the experiments reported in Table 1, nor can the effects of this partitioning be estimated. It constitutes a source of systematic modeling error that is intrinsic to all solubility and mixed fluid saturation models for silicate liquids; we expect the extent of this effect to increase with pressure and temperature.

Recovery of basaltic compositions is illustrated in ESM-Figs. 3d (Botcharnikov et al. 2005b), 3g (Dixon et al. 1995), 3m, 3o (Lesne et al. 2011a), 3n (Lesne et al. 2012b), 3r (Shishkina et al. 2010), 3s, 3u, 3v, 3y, and 3z (Shishkina et al. 2014). Model results are in good agreement with experiment except for those of Lesne et al. (2011a) at elevated pressure and two low-K<sub>2</sub>O compositions (169oxi and SC1) of Shishkina et al. (2014). The Lesne et al.’s (2011a) experimental compositions are S- and Cl-bearing and that may have a significant effect under high-*P* conditions. Shishkina et al.’s (2014) results for SC1 are at odds with results on the same bulk composition presented by Botcharnikov et al. (2005b).

The modeled high-pressure saturation curve for the ice-landite of Jakobsson (1997, ESM-Fig. 3j) underestimates melt CO<sub>2</sub> contents by about a factor of two. By contrast, the basaltic andesite of Morizet et al. (2010, ESM-Fig. 3q) is better recovered despite experiments being conducted under reducing conditions, which should displace the modeled saturation curves downward due to a lowering of the fugacity of CO<sub>2</sub>. Jakobsson’s results are somewhat enigmatic in that essentially the same CO<sub>2</sub> concentration is

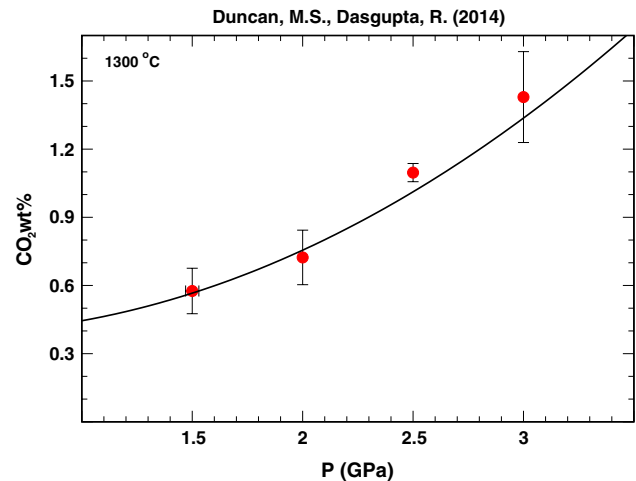


**Fig. 13** Modeled CO<sub>2</sub> solubility in average partial melt composition reported by Duncan and Dasgupta (2014) for a reported melt water content of ~0.45 wt%, plotted as a function of pressure. Experimental results are reported with two sigma brackets

measured over the entire documented range of melt water contents. He ascribes this result to a “high-pressure limit” on the capacity of the melt to dissolve CO<sub>2</sub>. Curiously, a similar constant CO<sub>2</sub> capacity is seen in the 500- and 200-MPa experiments of Botcharnikov et al. (2006) on an andesitic bulk composition (ESM-Fig. 3e, although note how the CO<sub>2</sub>-bearing array abruptly transitions to their experimental determinations of pure water solubility). By contrast, the Cl-bearing experiments of Botcharnikov et al. (2007, ESM-Fig. 3f) on the same andesitic composition can be viewed as consistent with the model curves, if allowance is made for the presence of Cl in system, which enhances water solubility by ~0.5 wt% (compare ESM-Figs. 3e and 3f at 200 MPa). Finally, modeled saturation curves at 1 GPa for Mt Hood andesite broadly account for the experimental results of King and Holloway (2002, ESM-Fig. 3k).

Mixed fluid experiments on dacitic bulk compositions (Behrens et al. 2004a, b, ESM-Fig. 3a) show that the model may slightly underpredict saturation pressures at low total pressure. By contrast, modeled results for rhyolitic liquids (Blank et al. 1993, ESM-Fig. 3c; Tamic et al. 2001, ESM-Figs. 3za and 3zb) are well described at 1100 °C for experiments at both 200 and 500 MPa. There is some indication that CO<sub>2</sub> solubility may be underpredicted by the model at low pressure (<200 MPa) and low water contents (<2 wt%), where total CO<sub>2</sub> concentrations are quite low. An important result, however, is that the very weak temperature dependence of saturation curve displacement documented by Tamic et al. (2001) is captured very well by the model. The experimental data of Duncan and Dasgupta (2014, Fig. 13) allow us to examine the extrapolation of the model to high pressure for rhyolitic compositions. These

experiments were performed on partial melts of sediments over the pressure range 1.5–3 GPa; the partial melts have compositions corresponding to high-alkali, low-silica rhyolites. Agreement between the modeled saturation curve and the experimental data is excellent (Fig. 13). Additionally, the model predicts that the dominant carbon species for these melts is molecular  $\text{CO}_2$ , consistent with FTIR analysis of quenched glass experimental run products (Duncan and Dasgupta 2014). This successful model extrapolation can be attributed to the quality of the low-temperature, low-pressure data (Blank et al. 1993; Tamic et al. 2001) upon which the standard-state volume and entropy of molecular  $\text{CO}_2$  are principally calibrated. Model agreement with the Duncan and Dasgupta (2014) data suggests that the large estimate for the molar volume of molecular  $\text{CO}_2$  (~4 J/bar, Table 2) is robust.

There are a large number of experimental studies on natural alkalic compositions ranging from alkali basalts to trachyandesites (Fig. 1c). Modeled saturation curves for basanites/tephrites (Shishkina et al. 2014, ESM-Figs. 3t, 3w) and trachybasalts (Shishkina et al. 2014, ESM-Fig. 3x; Lesne et al. 2011b, ESM-Fig. 3i) are well recovered, as are the shoshonitic composition of Vetere et al. (2011, ESM-Fig. 3zc; Vetere et al. 2014, ESM-Fig. 3zh), the Etna trachyandesite of Iacono-Marziano et al. (2012, ESM-Fig. 3h), and the latite of Vetere et al. (2014, ESM-Fig. 3zg). A number of experimental studies have been performed on phonotephrites. The Vesuvius lava of Lesne et al. (Lesne et al. 2011b, ESM-Fig. 3p) is modeled with fidelity over the pressure range 25–200 MPa, as is the Erebus lava of Iacono et al. (2013, ESM-Fig. 3i) and the three strongly alkali Alban Hills phonotephrites of Vetere et al. (2014, ESM-Figs. 3zd, 3ze, 3zf). Overall, the model recovers mixed fluid saturation relations very well in alkalic magmas, and this success must be ascribed in part to the extensive alkalic liquid-mineral data set that was available to calibrate the original MELTS liquid model. Previous comprehensive models of  $\text{H}_2\text{O}$ – $\text{CO}_2$  saturation (e.g., Papale et al. 2006), which have not benefitted from access to calibration data on more alkalic mixed fluid systems, are less successful than the proposed model in recovering results from these studies.

In general, experimental results in mixed fluid systems obtained at the highest pressures ( $\geq 500$  MPa) are more poorly recovered by the model than those at lower pressure, but there is also some inconsistency manifest in many studies between solubility measurements determined in  $\text{CO}_2$ -free fluid and saturation surfaces for mixed  $\text{H}_2\text{O}$ – $\text{CO}_2$  fluids at high pressure extrapolated to pure water (e.g., Behrens et al. 2009). The experimental complications at high pressure make these results subject to greater uncertainty (Moore 2008), but nonetheless, it is apparent that model results and experimental mixed fluid measurements are

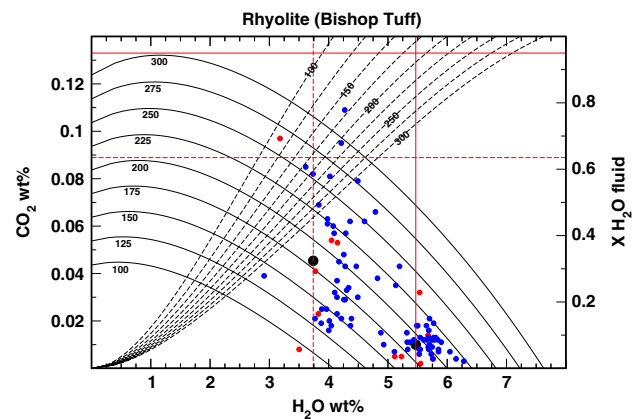


**Fig. 14** Model saturation curves for a bulk composition corresponding to an average late-erupted Bishop Tuff glass inclusion composition (Table 3). Solid curves are isobars (labeled in MPa) describing melt  $\text{CO}_2$  content (left vertical axis) as a function of  $\text{H}_2\text{O}$  content. Dashed curves are isobars of fluid  $\text{H}_2\text{O}$  mole fraction (right vertical axis). The graph is drawn for 750 °C. Available data on water and carbon dioxide contents from glass inclusions from both early-erupted (low  $\text{CO}_2$ , high  $\text{H}_2\text{O}$ ) and late-erupted (low  $\text{H}_2\text{O}$ , high and variable  $\text{CO}_2$ ) Bishop Tuff are plotted (Anderson et al. 2000, solid red circles; Wallace et al. 1995, 1999, solid blue circles). The average compositions of Anderson et al. (2000, large solid black circles) yield a pressure of ~180 MPa and associated fluid composition of ~0.95 for EBT and ~170 MPa with associated fluid composition of ~0.64 for LBT

generally in agreement at lower pressures (100–500 MPa) regardless of composition.

## Applications

The mixed fluid saturation model is explored by examining three applications. Water solubility and mixed fluid saturation state relations for rhyolitic liquids are first examined in light of observations from natural glass inclusions. Second, the mixed fluid saturation state model is coupled with rhyolite-MELTS to explore the consequences of fluid-saturated equilibrium and fractional crystallization of MORB. Finally, we use rhyolite-MELTS to calculate crystallization paths—including  $\text{H}_2\text{O}$  and  $\text{CO}_2$  evolution in the melt—and show how the results of modeling can be used to constrain the crystallization conditions and initial  $\text{H}_2\text{O}/\text{CO}_2$  ratios of natural magmas.

### Mixed fluid saturation in rhyolitic liquid

Figure 14 shows computed saturation curves for a high-silica rhyolite composition liquid, namely an average of late-erupted glass inclusions found in quartzes from the Bishop Tuff (see Table 3). Major-element compositions of glass inclusions in the Bishop Tuff are all very similar



**Table 3** Bulk compositions used in example calculations

	MORB <sup>a</sup>	Early Bishop Tuff <sup>b</sup>	Late Bishop Tuff <sup>b</sup>
SiO <sub>2</sub>	47.4	77.7	77.8
TiO <sub>2</sub>	1.01	0.08	0.09
Al <sub>2</sub> O <sub>3</sub>	17.64	12.5	12
Cr <sub>2</sub> O <sub>3</sub>	0.425		
Fe <sub>2</sub> O <sub>3</sub>	0.89	0.192	0.196
FeO	7.18	0.487	0.474
MgO	7.63	0.03	0.04
CaO	12.44	0.43	0.45
Na <sub>2</sub> O	2.65	3.99	3.7
K <sub>2</sub> O	0.03	4.89	5.36
P <sub>2</sub> O <sub>5</sub>	0.08		

<sup>a</sup> Allen et al. (1989)<sup>b</sup> Average compositions of melt inclusions compiled by Gualda et al. (2012a)

(see Gualda and Ghiorso 2013), particularly with respect to SiO<sub>2</sub> and Al<sub>2</sub>O<sub>3</sub> values, which makes the calculated saturation curves generally applicable to all Bishop Tuff glass inclusions plotted in Fig. 14. Solid curves in Fig. 14a show computed equilibrium CO<sub>2</sub>–H<sub>2</sub>O isobars over the pressure range 100–300 MPa. Melt CO<sub>2</sub> concentrations should be read from the left-scale of the ordinate. The dashed isobars show saturated fluid composition plotted as a function of melt water content; fluid composition should be read from the right scale of the ordinate, and the isobars migrate from left to right as pressure increases, as indicated. One characteristic feature of the H<sub>2</sub>O–CO<sub>2</sub> melt composition isobars is the maxima in melt CO<sub>2</sub> content found at low concentrations of dissolved water in the melt (and low  $X_{\text{H}_2\text{O}}^{\text{fluid}}$ ). A similar feature can be seen in all the model curves of all the compositions plotted in ESM-Fig. 3 and is universal for all compositions we have examined. The maxima at nonzero H<sub>2</sub>O values was in fact first observed by Eggler (1973) who explained it in terms of breakdown of polymerized melt structures (and hence enhancement of CO<sub>2</sub> solubility) due to dissolution of dissolved water to hydroxyl species. Holloway (1976) quantifies Eggler's explanation and suggests that the maximum should shift to higher  $X_{\text{H}_2\text{O}}^{\text{fluid}}$  with pressure. This shift is borne out by a number of experimental studies (e.g., Mysen 1976). In our model, the physical reason for the maxima is entropic and follows from Eggler's (1973) analysis. The enhanced solubility of CO<sub>2</sub> accompanying small additions of H<sub>2</sub>O arises because the activity of CO<sub>2</sub> in the melt is proportional to  $X_{\text{CO}_2}(1 - X_{\text{H}_2\text{O}})$  (see ESM Appendix; a Gibbs–Duhem consequence of  $a_{\text{H}_2\text{O}} \propto X_{\text{H}_2\text{O}}^2$ ); consequently, at fixed activity (fugacity) of CO<sub>2</sub>,  $X_{\text{CO}_2}$  must rise with the addition of water to the melt. At higher concentrations of dissolved water, however, strong preferential partitioning of CO<sub>2</sub> to the fluid phase

(Fig. 12) extracts CO<sub>2</sub> from the melt, and its concentration falls. Although our model contains a non-ideal positive mixing energy between dissolved H<sub>2</sub>O and both CO<sub>2</sub> and CaCO<sub>3</sub> melt species, the effect of that term is second order, and the maximum in the saturation curves would exist even if the energetics of mixing along the H<sub>2</sub>O–CO<sub>2</sub> component melt binary were ideal. The maximum in the saturation curves for mixed H<sub>2</sub>O–CO<sub>2</sub> fluid systems is a consequence of predominant hydroxyl speciation of dissolved water at low melt water contents.

Average H<sub>2</sub>O and CO<sub>2</sub> contents of glass inclusions from quartz phenocrysts in early and late eruptives of the Bishop Tuff are plotted in Fig. 14 (data from Wallace et al. 1999; Anderson et al. 2000). Model calculations reveal an average pressure of 190 MPa for entrapment of early-erupted inclusions and 180 MPa for late-erupted inclusions, and a total range of pressures that is similar for both early- and late-erupted rocks. Both these results are consistent with pressures derived using phase equilibria (Gualda and Ghiorso 2013, 2014), which suggests not only that these pressure estimates are robust, but also that both early-erupted and late-erupted magmas were fluid-saturated. Model fluid compositions are also consistent with previous studies, with early-erupted inclusions saturated with an essentially pure H<sub>2</sub>O vapor phase (5 mol% CO<sub>2</sub>) and the late-erupted inclusions saturated with a fluid containing about 36 mol% CO<sub>2</sub>. While the model curves are plotted assuming a temperature of 750 °C, the effect of temperature in displacing the isobars is minimal for rhyolite bulk composition (Tamic et al. 2001, see also ESM-Figs. 3za and 3zb); the saturation relations displayed in the figure should be valid over a temperature range of 650–850 °C.

### Fluid-saturated evolution of basaltic magma

One major goal in developing the model presented here resides in the desire to couple this fluid saturation model with the computational thermodynamics package rhyolite-MELTS in order to explore the consequences of fluid-saturated equilibrium and fractional crystallization of a magmatic system. Holloway (1976) has discussed in some detail the issues that arise in mixed fluid saturation and its effect on phase equilibria in granitic systems. Here, the problem of fluid saturation in systems evolving from initial MORB–liquid compositions will be assessed. This system is chosen for illustration because MORB phase relations are well understood, and the CO<sub>2</sub>-absent, H<sub>2</sub>O-bearing case has been modeled previously using MELTS (Ghiorso 1997).

An initial magma bulk composition is chosen (MORB, Table 3, column 1) with a dissolved volatile content of 0.8 wt% and weight ratio 3:1 (CO<sub>2</sub>/H<sub>2</sub>O). At 100 MPa, this composition is volatile-oversaturated at the liquidus.

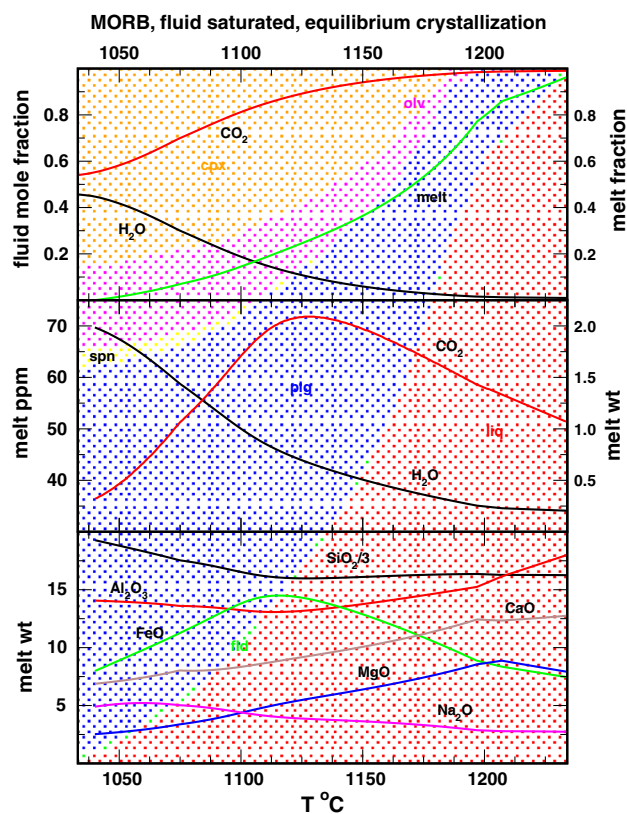


**Fig. 15** Equilibrium crystallization of fluid-saturated MORB liquid (Table 3, column 1). Calculations performed using rhyolite-MELTS (Gualda et al. 2012a) and the fluid saturation model developed in this paper. In order to maintain internal consistency between the fluid saturation model and rhyolite-MELTS, the CO<sub>2</sub> model extension developed in this paper was added to the existing water solubility model of rhyolite-MELTS. This addition insures that rhyolite-MELTS recovers correctly the effect of water on the invariant point for silicic systems, but also allows for partitioning of CO<sub>2</sub> between melt and fluid phase to be consistently modeled. By not using the revised water solubility model, calculations coupled to rhyolite-MELTS do not take full advantage of the improved recovery of water solubility provided by that model, but for low-alkali natural liquids, these improvements are minor and generally within experimental uncertainty. The background in the figure shows relative mass proportions of phases with fields labeled as: liq = liquid, fld = fluid, plg = plagioclase, spn = Fe–Ti oxide, olv = olivine, cpx = clinopyroxene. *Top panel* evolution of fluid composition (red and black curves, left axis) and liquid fraction (green curve, right axis). *Middle panel*: evolution of melt volatile content; H<sub>2</sub>O in wt% (black curve, right axis), CO<sub>2</sub> in ppm (red curve, left axis). *Lower panel*: evolution of melt composition; note scaling of silica concentration

Three simulations were performed: (1) isobaric equilibrium crystallization to the solidus, (2) isobaric fractional crystallization of solid phases with the possibility of back reaction with the fluid phase, and (3) isobaric fractional crystallization of both solid and fluid phases. The second model is explored to consider the scenario of chemical isolation of the interiors of growing phenocrysts without the necessity of physical separation of phases from liquid. The third

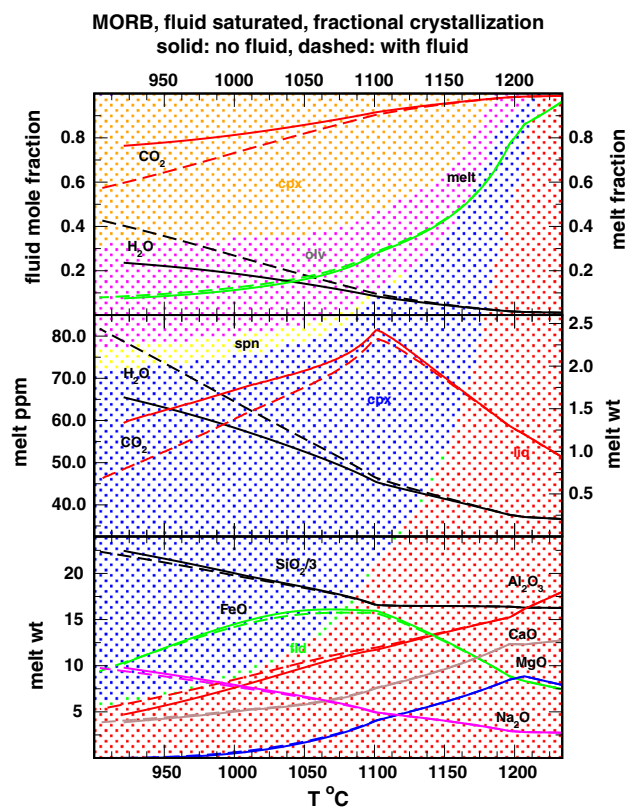


**Fig. 16** Fractional crystallization of fluid-saturated MORB liquid (Table 3, column 1). Calculations performed using rhyolite-MELTS as described in the caption for Fig. 15, which should also be consulted for the explanation of symbols. *Solid curves* denote calculations where solid phases are chemically isolated from the evolving magma but fluid is kept in chemical communication. *Dashed curves* reflect calculations where both solid and fluid phases are prevented from backreacting with the liquid as crystallization proceeds

model considers the same scenario with transport of bubbles of fluid out of the system at a rate exceeding that of crystal growth.

Results of the simulations are reported in Figs. 15 and 16. Comparing all three simulations to model calculations presented in Ghiorso (1997) shows that the presence of CO<sub>2</sub> in the system does not substantially affect the phase relations other than inducing volatile saturation early in the evolution. In all three cases, the initial fluid that forms has a composition that is essentially pure CO<sub>2</sub>. The fluid evolves to become more H<sub>2</sub>O-rich as the system crystallizes, but even near the solidus, the fluid contains >50 mol% CO<sub>2</sub>. By contrast, the concentrations of H<sub>2</sub>O and CO<sub>2</sub> dissolved in the melt show a more complex temperature dependence. In the initial stages of crystallization, the abundance of both volatile components increases, CO<sub>2</sub> more so than H<sub>2</sub>O. At the onset of the crystallization of spinel, which drives silica content of the melt to higher values, the increasing trend of CO<sub>2</sub> enrichment reverses, and ultimately, melt

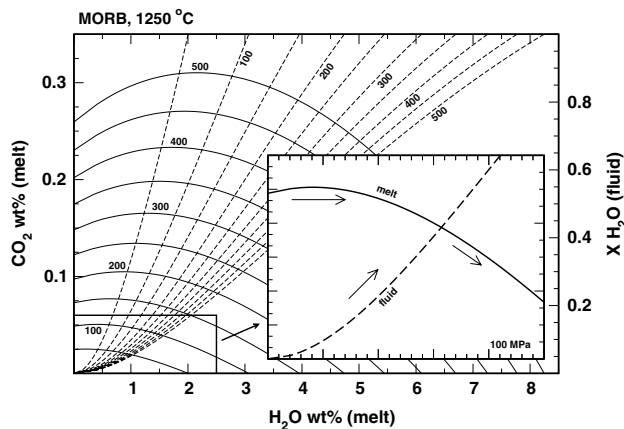


**Fig. 17** Model saturation surfaces for a bulk composition MORB liquid (see Table 3, column 1). *Solid curves* are isobars (labeled in MPa) of melt  $\text{CO}_2$  content (*left vertical axis*) versus melt  $\text{H}_2\text{O}$  content. *Dashed curves* are isobars of fluid  $\text{H}_2\text{O}$  mole fraction (*right vertical axis*). The graph is drawn for 1250 °C. The 100 MPa saturation relations are detailed in the blowup *inset*, with *arrows* indicating the direction of evolution of a magma degassing and initially saturated with a fluid very enriched in  $\text{CO}_2$

$\text{CO}_2$  concentrations are driven to lower values as the system evolves. The initial trend of  $\text{CO}_2$  enrichment may seem contradictory to the expected evolution along mixed fluid saturation curves, which for this MORB are plotted in Fig. 17. As the fluid coexisting with melt becomes more water-rich, we expect the melt to also become enriched in  $\text{H}_2\text{O}$ , but we also expect  $\text{CO}_2$  concentration to decrease. This is because as  $\text{CO}_2$  and  $\text{H}_2\text{O}$  are partitioned into the fluid phase, the fluid composition broadly follows the 100-MPa fluid isobar (dashed curve, Fig. 17, see inset) toward higher  $X_{\text{H}_2\text{O}}^{\text{fluid}}$ , at the same time, the melt becomes enriched in  $\text{H}_2\text{O}$ , in part due to the partitioning of  $\text{CO}_2$  out of the melt into the fluid phase, and in part because the mass of solid phases crystallizing exceeds the mass of exsolved fluid. As the magma evolves by crystallization, the melt loses  $\text{CO}_2$  and its volatile content should follow the melt isobar (solid curves, Fig. 17). Necessarily, the fluid that coexists with the melt under these conditions must become more  $\text{H}_2\text{O}$ -rich. In detail, however, there are nuances to this evolution trend. At the initial stages of crystallization, the concentration of dissolved  $\text{CO}_2$  increases because of the maximum in the saturation curve, but this effect is minor at low pressure. The driving force for the increase in the concentration of dissolved  $\text{CO}_2$  in the MORB crystallization case is the melt bulk composition change that involves a rise in the concentration of both FeO and  $\text{Na}_2\text{O}$ , the effect of which increases the capacity of the melt to retain  $\text{CO}_2$ . Once spinel appears on the liquidus, however, silica increases and the FeO content decreases, and together these changes in bulk composition lower the capacity of the melt to hold carbon dioxide.

In the case of solid + fluid phase fractionation (Fig. 16, dashed curves),  $\text{H}_2\text{O}$  concentration in the exsolved fluid rises more dramatically in the later stages of crystallization than the solid-only case; bear in mind that what is plotted in Fig. 16 is the instantaneous fluid composition and *not* the cumulative composition of fluid fractionate. The cause for this increase is due to the dramatic change in melt volatile composition as  $\text{CO}_2$ -rich bubbles are discarded from the magma and is in contrast to the more muted increase observed for the equilibrium crystallization or the solid-phase-only fractionation case. The  $\text{H}_2\text{O}$  concentration in the melt phase rises appreciably in the fluid fractionation case because  $\text{CO}_2$  is being preferentially withdrawn from the system. Remarkably, the highest  $\text{CO}_2$  melt concentrations are generated for the fractionation case where fluid is maintained in chemical equilibrium with the melt. The evolution of melt  $\text{H}_2\text{O}$  and  $\text{CO}_2$  concentrations clearly distinguishes the three endmember modes of crystallization simulated in Figs. 15 and 16, and it is intriguing to speculate that these distinct volatile trends may be captured in trapped glass inclusions and therefore used to constrain some details of the history of crystallizing magmas.

#### Geobarometry using the simultaneous equilibrium between melt, quartz, feldspars, and a fluid phase

Much attention has been given to the estimation of pressures using  $\text{H}_2\text{O}$ – $\text{CO}_2$  fluid saturation in rhyolitic melts. Results presented in Fig. 14 suggest entrapment pressures close to 180 MPa for the average late-erupted glass inclusion composition from the Bishop Tuff. We have recently proposed a method whereby the simultaneous equilibrium of melt, quartz, feldspars, and fluid can be used to estimate the crystallization pressure of rocks for which melt composition can be estimated—we refer to this method as the rhyolite-MELTS geobarometer (Gualda and Ghiorso 2013, 2014). The mixed  $\text{H}_2\text{O}$ – $\text{CO}_2$  model presented here allows us to explicitly evaluate the effect of  $\text{CO}_2$  on the application of the rhyolite-MELTS geobarometer (the effect can be implicitly tested by varying  $\text{H}_2\text{O}$  content, as performed in Gualda and Ghiorso 2013, 2014). We use here the same average late-erupted glass composition employed by Gualda et al. (2012a; calculated from data of Anderson et al. 2000; see also Gualda and Ghiorso 2013; also Table 3). We vary  $\text{H}_2\text{O}$  above and below the average glass inclusion value of 3.74 wt%  $\text{H}_2\text{O}$ , from 2.74 to 4.74 in 0.5 increments. We use initial values of 0, 10, 20, 50, 100, 200, 500, and 1000 ppm  $\text{CO}_2$ . We thus apply the rhyolite-MELTS geobarometer to a total of 40 compositions (5  $\text{H}_2\text{O}$  values  $\times$  8  $\text{CO}_2$  values). It is clear from the results (Fig. 18) that the derived pressures are entirely insensitive to the choice of initial  $\text{CO}_2$  concentration. This conclusion emerges from the fact that the position of the

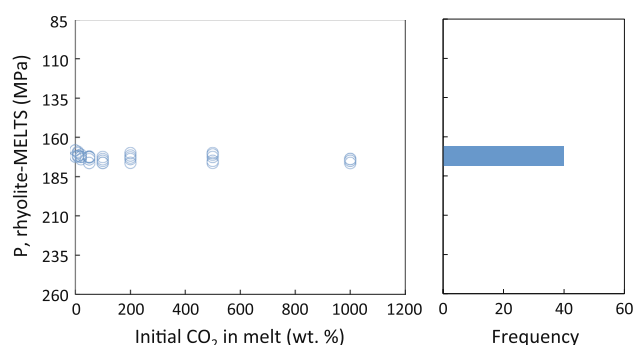


**Fig. 18** Pressures estimated using the rhyolite-MELTS geobarometer (Gualda and Ghiorso 2014) for average late-erupted bulk pumice composition of Hildreth (1979). Five different initial H<sub>2</sub>O contents (4.47, 4.97, 5.47, 5.97, 6.47 wt% H<sub>2</sub>O) and eight different CO<sub>2</sub> contents (0, 10, 20, 50, 100, 200, 500, 1000 ppm CO<sub>2</sub>) are used, resulting in a total of 40 pressure estimates. The calculations establish the insensitivity of pressure estimates for quartz–feldspar-bearing magmas to water and CO<sub>2</sub> content of the magma

quartz–feldspar cotectic surface is fundamentally dependent on the total pressure, with only a weak dependency on water pressure for values below ~3 wt% H<sub>2</sub>O (Gualda and Ghiorso 2013, 2014). In this context, CO<sub>2</sub>—a trace element in the melt phase—plays no direct role in the stability of quartz or feldspar; instead, CO<sub>2</sub> buffers the activity—and thus the concentration—of H<sub>2</sub>O in the melt. With this perspective, the results presented here are largely unsurprising and reinforce the conclusion of Gualda and Ghiorso (2013) that late-erupted glass inclusions were entrapped under fluid-saturated conditions at pressures of ~175 MPa.

### Crystallization paths of a high-silica rhyolite under variable H<sub>2</sub>O and CO<sub>2</sub>

The evolution of H<sub>2</sub>O and CO<sub>2</sub> in rhyolitic magmas has received significant attention given the wealth of information that can be derived from H<sub>2</sub>O–CO<sub>2</sub> data on glass inclusions (e.g., Wallace et al. 1999, among many others). Typically, glass inclusion data are interpreted considering H<sub>2</sub>O–CO<sub>2</sub> saturation curves (e.g., Blundy et al. 2010 and references therein, among many others), but it is difficult to appropriately consider the evolution in the crystallizing assemblage that accompanies the evolution in H<sub>2</sub>O–CO<sub>2</sub> in the melt phase. We use rhyolite-MELTS coupled with the mixed fluid model developed here to illustrate this relationship for a high-silica rhyolite pumice composition representative of the late-erupted Bishop Tuff (from Hildreth 1979). Simulations for this composition for the water-saturated case were presented elsewhere (Gualda et al. 2012a, b). The analysis is not exhaustive and intended only to demonstrate the capabilities of the coupling of

rhyolite-MELTS with a mixed fluid model, as well as the challenges in establishing appropriate initial conditions and styles of crystallization (equilibrium versus fractional crystallization, for instance).

One of the challenges in such modeling is that, while glass inclusions provide snapshots of melt compositions attained during crystallization (and inferred fluid compositions obtained using saturation models like the one presented here), we lack detailed knowledge of the initial H<sub>2</sub>O and CO<sub>2</sub> contents of magmas. Our approach here is to use a wide range of H<sub>2</sub>O and CO<sub>2</sub> initial values to investigate the simultaneous effect of crystallization and H<sub>2</sub>O–CO<sub>2</sub> evolution in the melt and fluid. We use a reference H<sub>2</sub>O value in the melt of 3.74 wt% (same as above), and we again vary initial melt H<sub>2</sub>O relative to this value from 2.74 to 4.74 wt% in 0.5 increments. We use initial CO<sub>2</sub> values of 0–1000 ppm CO<sub>2</sub>, resulting in 40 simulations, which leads to a number of different fluid-saturated and fluid-undersaturated evolution paths. We use a crystallization pressure of 175 MPa, consistent with the glass inclusion data (see above, also Gualda et al. 2012a; Gualda and Ghiorso 2013). For simplicity, we did not consider fluid fractionation, but we emphasize that it would be possible to do so using rhyolite-MELTS.

One important caveat in the application of the mixed fluid model coupled with rhyolite-MELTS is that a compromise is necessary to render the H<sub>2</sub>O–CO<sub>2</sub> model developed here consistent with the quartz–two-feldspar cotectic calibration in rhyolite-MELTS. This cotectic was calibrated by Gualda et al. (2012a) to be internally consistent with the *original* MELTS water solubility model. The new water solubility model proposed here disrupts that calibration. As mentioned above, the best solution to this dilemma would involve recalibration of the cotectic against mixed fluid-phase equilibrium data. Unfortunately, at this juncture, the data available to perform this task are insufficient, and the project to acquire them and recalibrate the phase equilibrium model would exceed the scope of this paper. The compromise we choose is to keep the water solubility model in rhyolite-MELTS unmodified, and to couple it to the CO<sub>2</sub> and mixed fluid saturation model presented here. Or, in other words, to replace the new endmember water solubility model with the older MELTS model, but adopt the CO<sub>2</sub> model and mixed fluid model developed above. The negative consequence of this compromise is that H<sub>2</sub>O concentrations in the melt phase are slightly underestimated for cotectic bulk compositions. The positive consequence is that solid–liquid phase relations at the cotectic are correctly recovered, and the effect of the addition of CO<sub>2</sub> to the melt and fluid phase is properly extended. With this compromise, we can still explore the coevolution of melt H<sub>2</sub>O and CO<sub>2</sub>



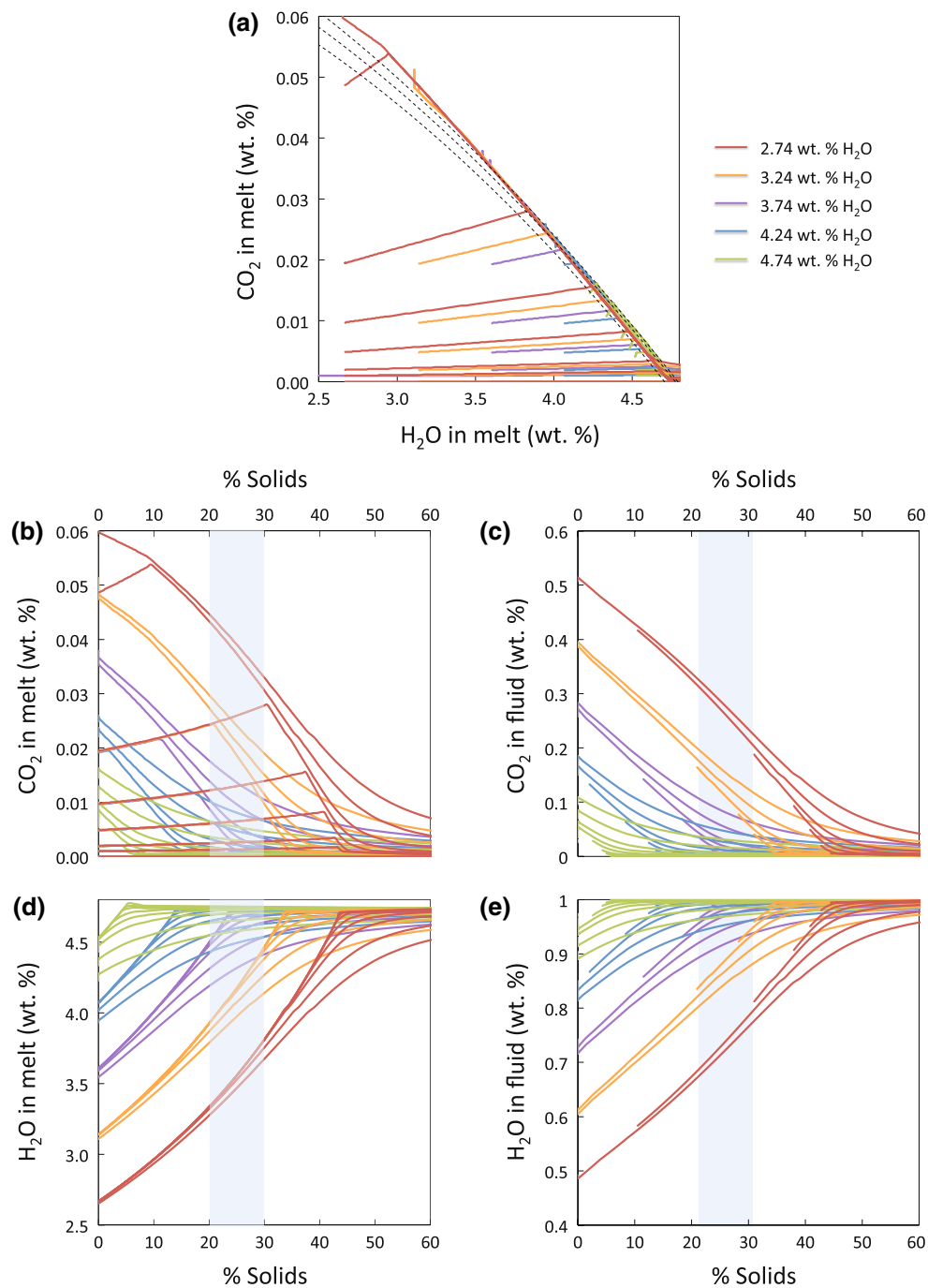


**Fig. 19** Crystallization paths for average late-erupted bulk pumice composition of Hildreth (1979; see Table 3). Five different initial H<sub>2</sub>O contents (4.47, 4.97, 5.47, 5.97, 6.47 wt% H<sub>2</sub>O) and eight different CO<sub>2</sub> contents (0, 10, 20, 50, 100, 200, 500, 1000 ppm CO<sub>2</sub>) are used, resulting in a total of 40 simulations. All simulations were conducted at 175 MPa, with oxygen fugacity buffered at the Ni–NiO

buffer. *Top panel* (a) shows the evolution of melt H<sub>2</sub>O and CO<sub>2</sub> contents in the magma along the 40 crystallization paths. *Left and right panels* show the evolution paths in terms of H<sub>2</sub>O(melt)—% solid, H<sub>2</sub>O(fluid)—% solid. *Colors* correspond to initial bulk water content, as indicated. The *shaded area* represents the extent of crystallization recorded in late-erupted Bishop Tuff pumice

concentrations and the abundance and composition of all phases present including fluid concentrations and fluid saturation pressures. Importantly, this compromise need

only be made for recovery of phase relations in quartz-two-feldspar cotectic compositions. In other bulk compositions, MELTS crystallization simulations may be

performed utilizing the fully internally consistent mixed fluid model proposed in this paper.<sup>4</sup>

The results of the simulations using the average late-erupted Bishop Tuff pumice composition are shown in Fig. 19. The evolution of  $\text{H}_2\text{O}$ – $\text{CO}_2$  in the melt is shown in the top panel (Fig. 19a) and as a function of the abundance of coexisting solids in the left panels (Fig. 19b, d), while the relationship between the evolution of fluid  $\text{CO}_2$  and  $\text{H}_2\text{O}$  as a function of the abundance of coexisting solids is shown in the right panels (Fig. 19c, e). Evolution curves are color-coded according to their initial  $\text{H}_2\text{O}$  concentration. The typical crystallinity of late-erupted Bishop Tuff pumice (~20–30 wt%) is indicated by the shaded regions (Fig. 19b–e). In all cases,  $\text{H}_2\text{O}$  concentration in the melt increases steadily up to a value of ~4.7 wt%  $\text{H}_2\text{O}$ , which corresponds to the  $\text{CO}_2$ -free solubility of  $\text{H}_2\text{O}$  calculated by the rhyolite-MELTS water model. For fluid-saturated conditions,  $\text{CO}_2$  in the melt decreases steadily; for fluid-undersaturated conditions,  $\text{CO}_2$  concentrations rise slightly until fluid saturation takes place, from which point the evolution is the same as the fluid-saturated case. The evolution of the fluid-phase composition parallels that of the melt: paths are largely dictated by the initial  $\text{H}_2\text{O}$  concentration, with  $\text{CO}_2$  controlling the point at which fluid saturation takes place. For the initial conditions considered here, the maximum  $\text{CO}_2$  concentration in the melt is ~600 ppm, and concentrations of ~500 ppm, as observed in late-erupted Bishop Tuff inclusions (Wallace et al. 1999; Anderson et al. 2000), can only be attained with relatively high initial  $\text{CO}_2$  (>500 ppm) and low initial  $\text{H}_2\text{O}$  (<3.24 wt%). The observation that crystallinity (i.e., % solids) in pumice is between 20 and 30 wt% further limits the range of possible starting  $\text{H}_2\text{O}$  concentrations to the lowest values considered here (2.74 wt%).

## Summary

A thermodynamic model is developed for  $\text{H}_2\text{O}$ – $\text{CO}_2$  mixed fluid saturation in natural silicate liquids. The model replaces the water saturation calibration and extends the anhydrous liquid thermodynamic model of MELTS (Ghiorso and Sack 1995) and rhyolite-MELTS (Gualda et al. 2012a). The model is intended to be used at lower pressures (<1 GPa) and on relatively oxidized systems, such that all carbon in the system is assumed to be  $\text{C}^{4+}$ . The model assumes an entropic contribution to the melt that is

consistent with water dissolution as hydroxyl units and with carbon dioxide dissolving as both molecular and carbonate species. Excess enthalpy terms are calibrated from experimental measurements and in part compensate for any assumptions regarding melt speciation. The model is internally consistent with thermodynamic properties of the fluid phase reported in Duan and Zhang (2006). As the model is built upon MELTS, calculations utilizing that code can now be made to examine  $\text{H}_2\text{O}$  and  $\text{CO}_2$  partitioning between the melt and vapor phase accompanying crystallization along a specified temperature and pressure evolution path.

## Availability

The saturation model described in this paper is available as a Macintosh and iPad application from the Apple App store, and as a Web-based calculator at [ctserver.ofm-research.org](http://ctserver.ofm-research.org). An enhanced version of rhyolite-MELTS that contains the mixed fluid model developed in this paper is available from the Web site at [melts.ofm-research.org](http://melts.ofm-research.org).

**Acknowledgments** We are indebted to Gordon Moore for his helpful guidance, sage advice, and thoughtful insights. Three reviewers provided important and stimulating criticism that greatly improved the paper. In particular, the comments and suggestions of Roman Botcharnikov were especially helpful and directly instigated the metamorphosis of a mediocre first attempt into, we trust, a more useful and meaningful paper. Roman as well as Francesco Vetere generously shared experimental data prior to publication. Material support for this investigation was provided by the National Science Foundation through awards EAR 09-48734, EAR 11-19297, and EAR 13-21924 to MSG and EAR 09-48528, EAR 11-51337, and EAR 13-21806 to GARG.

## References

- Allen JF, Batiza R, Perfit MR, Fornari DJ, Sack RO (1989) Petrology of lavas from the Lamont seamount chain and adjacent East Pacific Rise, 10°N. *J Petrol* 30:1245–1298
- Anderson AT, Davis AM, Lu FQ (2000) Evolution of Bishop Tuff rhyolitic magma based on melt and magnetite inclusions and zoned phenocrysts. *J Petrol* 41:449–473
- Barclay J, Rutherford MJ, Carroll MR, Murphy MD, Devine JD, Gardner J, Sparks RSJ (1998) Experimental phase equilibria constraints on pre-eruptive storage conditions of the Soufriere Hills magma. *Geophys Res Lett* 25:3437–3440
- Behrens H (1995) Determination of water solubilities in high-viscosity melts: an experimental study on  $\text{NaAlSi}_3\text{O}_8$  and  $\text{KAlSi}_3\text{O}_8$  melts. *Eur J Mineral* 7:905–920
- Behrens H, Jantos N (2001) The effect of anhydrous composition on water solubility in granitic melts. *Am Mineral* 86:14–20
- Behrens H, Nowak M (1997) The mechanisms of water diffusion in polymerized silicate melts. *Contrib Mineral Petrol* 126:377–385
- Behrens H, Meyer M, Holtz F, Benne D, Nowak M (2001) The effect of alkali ionic radius, temperature, and pressure on the solubility of water in  $\text{MAlSi}_3\text{O}_8$  melts (M = Li, Na, K, Rb). *Chem Geol* 174:275–289

<sup>4</sup> An updated version of rhyolite-MELTS may be downloaded from [melts.ofm-research.org](http://melts.ofm-research.org) that implements both the compromised mixed fluid model, which is suitable for quartz-two-feldspar cotectic compositions, and the full mixed fluid model, which is applicable to other natural magma compositions.



- Behrens H, Ohlhorst S, Holtz F, Champenois M (2004a)  $\text{CO}_2$  solubility in dacitic melts equilibrated with  $\text{H}_2\text{O}$ – $\text{CO}_2$  fluids: implications for modeling the solubility of  $\text{CO}_2$  in silicic melts. *Geochim Cosmochim Acta* 68:4687–4703
- Behrens H, Tamic N, Holtz F (2004b) Determination of the molar absorption coefficient for the infrared absorption band of  $\text{CO}_2$  in rhyolitic glasses. *Am Mineral* 89:301–306
- Behrens H, Misiti V, Freda C, Vetere F, Botcharnikov RE, Scarlato P (2009) Solubility of  $\text{H}_2\text{O}$  and  $\text{CO}_2$  in ultrapotassic melts at 1200 and 1250 °C and pressure from 50 to 500 MPa. *Am Mineral* 94:105–120
- Benne D, Behrens H (2003) Water solubility in haplobasaltic melts. *Eur J Mineral* 15:803–814
- Berndt J, Liebske C, Holtz F, Freise M, Nowak M, Ziegenbein D, Hurkuk W, Koepke J (2002) A combined rapid-quench and  $\text{H}_2$ -membrane setup for internally heated pressure vessels: description and application for water solubility in basaltic melts. *Am Mineral* 87:1717–1720
- Bezmen NI, Zharikov VA, Epelbaum MB, Zavel'sky VO, Dikov YP, Suk N, Koshemchuk SK (1991) The system  $\text{NaAlSi}_3\text{O}_8$ – $\text{H}_2\text{O}$ – $\text{H}_2$  (1200 °C, 2-kbar)—the solubility and interaction mechanism of fluid species with melt. *Contrib Mineral Petrol* 109:89–97
- Blank JG, Stolper EM, Carroll MR (1993) Solubilities of carbon dioxide and water in rhyolitic melt at 850 °C and 750 bars. *Earth and Planet Sci Lett* 119:27–36
- Blatter DW, Carmichael ISE (2001) Hydrous phase equilibria of a Mexican high-silica andesite: a candidate for a mantle origin? *Geochim Cosmochim Acta* 65:4043–4065
- Blundy J, Cashman K, Rust A, Witham F (2010) A case for  $\text{CO}_2$ -rich arc magmas: *Earth Planet Sci Lett* 290:289–301. doi:10.1016/j.epsl.2009.12.013
- Botcharnikov R, Freise M, Holtz F, Behrens H (2005a) Solubility of C–O–H mixtures in natural melts: new experimental data and application range of recent models. *Ann Geophys* 48:633–646
- Botcharnikov R, Koepke J, Holtz F, McCammon C, Wilke M (2005b) The effect of water activity on the oxidation and structural state of Fe in a ferro-basaltic melt. *Geochim Cosmochim Acta* 69:5071–5085
- Botcharnikov RE, Behrens H, Holtz F (2006) Solubility and speciation of C–O–H fluids in andesitic melt at  $T = 1100$ – $1300$  °C and  $P = 200$  and 500 MPa. *Chem Geol* 229:125–143
- Botcharnikov RE, Holtz F, Behrens H (2007) The effect of  $\text{CO}_2$  on the solubility of  $\text{H}_2\text{O}$ –Cl fluids in andesitic melt. *Eur J Mineral* 19:671–680
- Brey GP (1976)  $\text{CO}_2$  solubility and solubility mechanisms in silicate melts at high pressures. *Contrib Mineral Petrol* 57:215–221
- Brooker R, Kohn S, Holloway J, McMillan P, Carroll M (1999) Solubility, speciation and dissolution mechanisms for  $\text{CO}_2$  in melts on the  $\text{NaAlO}_2$ – $\text{SiO}_2$  join. *Geochim Cosmochim Acta* 63:3549–3565
- Brooker R, Kohn S, Holloway J, McMillan P (2001) Structural controls on the solubility of  $\text{CO}_2$  in silicate melts part I: bulk solubility data. *Chem Geol* 174:225–239
- Burnham CW, Davis N (1974) The role of  $\text{H}_2\text{O}$  in silicate melts; II. Thermodynamic and phase relations in the system  $\text{NaAlSi}_3\text{O}_8$ – $\text{H}_2\text{O}$  to 10 kilobars, 700 degrees to 1100 degrees C. *Am J Sci* 274:902–940
- Burnham C, Jahns R (1962) A method for determining the solubility of water in silicate melts. *Am J Sci* 260:721–745
- Burnham CW, Holloway JR, Davis NF (1969) Thermodynamic properties of water to 1000 °C and 10000 bars. *Geol Soc Am Spec Pap* 132:1–96
- Carroll M, Blank JG (1997) The solubility of  $\text{H}_2\text{O}$  in phonolitic melts. *Am Mineral* 82:549–556
- Di Matteo V, Carroll M, Behrens H, Vetere F, Brooker R (2004) Water solubility in trachytic melts. *Chem Geol* 213:187–196
- Dingwell DB, Harris DM, Scarfe CM (1984) The solubility of  $\text{H}_2\text{O}$  in melts in the system  $\text{SiO}_2$ – $\text{Al}_2\text{O}_3$ – $\text{Na}_2\text{O}$ – $\text{K}_2\text{O}$  at 1-kbar to 2-kbar. *J Geol* 92:387–395
- Dingwell DB, Holtz F, Behrens H (1997) The solubility of  $\text{H}_2\text{O}$  in peralkaline and peraluminous granitic melts. *Am Mineral* 82:434–437
- Dixon J, Stolper E, Holloway J (1995) An experimental study of water and carbon dioxide solubilities in mid-ocean ridge basaltic liquids. Part I: calibration and solubility models. *J Petrol* 36:1607–1631
- Duan X (2014) A general model for predicting the solubility behavior of  $\text{H}_2\text{O}$ – $\text{CO}_2$  fluids in silicate melts over a wide range of pressure, temperature and compositions. *Geochim Cosmochim Acta* 125:582–609
- Duan Z, Zhang Z (2006) Equation of state of the  $\text{H}_2\text{O}$ ,  $\text{CO}_2$ , and  $\text{H}_2\text{O}$ – $\text{CO}_2$  systems up to 10 GPa and 2573.15 K: molecular dynamics simulations with ab initio potential surface. *Geochim Cosmochim Acta* 70:2311–2324
- Duncan MS, Agee CB (2011) The partial molar volume of carbon dioxide in peridotite partial melt at high pressure. *Earth Planet Sci Lett* 312:429–436
- Duncan MS, Dasgupta R (2014)  $\text{CO}_2$  solubility and speciation in rhyolitic sediment partial melts at 1.5–3.0 GPa—implications for carbon flux in subduction zones. *Geochim Cosmochim Acta* 124:328–347
- Eggler DH (1973) Role of  $\text{CO}_2$  in melting processes in the mantle. *Yearb Carnegie Inst Wash* 72:457–467
- Feig ST, Koepke J, Snow JE (2006) Effect of water on tholeiitic basalt phase equilibria: an experimental study under oxidizing conditions. *Contrib Mineral Petrol* 152:611–638
- Fine G, Stolper EM (1985) The speciation of carbon dioxide in sodium aluminosilicate melts. *Contrib Mineral Petrol* 91:105–121
- Fine G, Stolper EM (1986) Dissolved carbon dioxide in basaltic glasses: concentrations and speciation. *Earth Planet Sci Lett* 76:263–278
- Fogel RA, Rutherford M (1990) The solubility of carbon-dioxide in rhyolitic melts—a quantitative FTIR study. *Am Mineral* 75:1311–1326
- Gaillard F, Pichavant M, Scaillet B (2003) Experimental determination of activities of  $\text{FeO}$  and  $\text{Fe}_2\text{O}_3$  components in hydrous silicic melts under oxidizing conditions. *Geochim Cosmochim Acta* 67:4389–4409
- Gerke TL, Kilinc AI (1992) Enrichment of  $\text{SiO}_2$  in rhyolites by fractional crystallization: an experimental study of peraluminous granitic rocks from the St. Francois Mountains, Missouri, USA. *Lithos* 29:273–283
- Ghiorso MS (1997) Thermodynamic modeling of igneous processes. *Annual Rev Earth Planet Sci* 25:221–241
- Ghiorso MS, Sack RO (1995) Chemical mass transfer in magmatic processes IV. A revised and internally consistent thermodynamic model for the interpolation and extrapolation of liquid–solid equilibria in magmatic systems at elevated temperatures and pressures. *Contrib Mineral Petrol* 119:197–212
- Ghiorso MS, Carmichael ISE, Rivers ML, Sack RO (1983) The Gibbs free energy of mixing of natural silicate liquids; an expanded regular solution approximation for the calculation of magmatic intensive variables. *Contrib Mineral Petrol* 84:107–145
- Ghiorso MS, Hirschmann MM, Reiners PW, Kress VC III (2002) The pMELTS: a revision of MELTS for improved calculation of phase relations and major element partitioning related to partial melting of the mantle to 3 GPa. *Geochim Geophys Geosyst*. doi:10.1029/2001GC000217
- Giordano D, Russell JK, Dingwell DB (2008) Viscosity of magmatic liquids: a model. *Earth Planet Sci Lett* 271:123–134

- Grove TL, Donnelly-Nolan JM, Housh T (1997) Magmatic processes that generated the rhyolite of Glass Mountain, Medicine Lake volcano, N. California. *Contrib Mineral Petrol* 127:205–223
- Gualda GAR, Ghiorso MS (2013) The Bishop Tuff giant magma body: an alternative to the standard model. *Contrib Mineral Petrol* 166:755–775
- Gualda GAR, Ghiorso MS (2014) Phase-equilibrium geobarometers for silicic rocks based on rhyolite-MELTS. Part 1: principles, procedures, and evaluation of the method. *Contrib Mineral Petrol* 168:1033. doi:10.1007/s00410-014-1033-3
- Gualda GAR, Ghiorso MS, Lemons RV, Carley TL (2012a) Rhyolite-MELTS: a modified calibration of MELTS optimized for silica-rich, fluid-bearing magmatic systems. *J Petrol* 53:875–890
- Gualda GAR, Pamukcu AS, Ghiorso MS, Anderson AT Jr, Sutton SR, Rivers ML (2012b) Timescales of quartz crystallization and the longevity of the Bishop giant magma body. *PLoS One* 7:e37492
- Guillot B, Sator N (2011) Carbon dioxide in silicate melts: a molecular dynamics simulation study. *Geochim Cosmochim Acta* 75:1829–1857
- Haar L, Gallagher JS, Kell GS (1984) NBS/NRC steam tables. Thermodynamic and transport properties and computer programs for vapor and liquid states of water in SI units. Hemisphere, Washington, DC, pp 271–276
- Hamilton D, Oxtoby S (1986) Solubility of water in albite-melt determined by the weight-loss method. *J Geol* 94:626–630
- Hamilton D, Burnham C, Osborn E (1964) The solubility of water and effects of oxygen fugacity and water content on crystallization in mafic magmas. *J Petrol* 5:21–39
- Hammer JE, Rutherford MJ, Hildreth W (2002) Magma storage prior to the 1912 eruption at Novarupta, Alaska. *Contrib Mineral Petrol* 144:144–162
- Helgeson HC, Kirkham DH (1974) Theoretical prediction of the thermodynamic behavior of aqueous electrolytes at high pressures and temperatures. I. Summary of the thermodynamic/electrostatic properties of the solvent. *Am J Sci* 274:1089–1198
- Hildreth W (1979) The Bishop Tuff: evidence for the origin of compositional zonation in silicic magma chambers. *Geol Soc Am Spec Pap* 180:43–75
- Hirschmann MM, Ghiorso MS, Davis FA, Gordon SM, Mukerjee S, Grove TL, Krawczynski M, Medard E, Till CB (2008) Library of experimental phase relations (LEPR): a database and web portal for experimental magmatic phase equilibria. *Geochim Geophys Geosys* 9:Q03011. doi:10.1029/2007GC001894
- Holloway JR (1976) Fluids in the evolution of granitic magmas: consequences of finite CO<sub>2</sub> solubility. *Geol Soc Am Bull* 10:1513–1518
- Holtz F, Behrens H, Dingwell DB, Taylor R (1992) Water solubility in aluminosilicate melts of haplogranite composition at 2 kbar. *Chem Geol* 96:289
- Holtz F, Behrens H, Dingwell DB, Johannes W (1995) H<sub>2</sub>O solubility in haplogranitic melts; compositional, pressure, and temperature dependence. *Am Mineral* 80:94
- Holtz F, Roux J, Behrens H, Pichavant M (2000) Water solubility in silica and quartzofeldspathic melts. *Am Mineral* 85:682–686
- Hui H, Zhang Y, Xu Z, Behrens H (2008) Pressure dependence of the speciation of dissolved water in rhyolitic melts. *Geochim Cosmochim Acta* 72:3229–3240
- Iacono-Marziano G, Gaillard F, Pichavant M (2008) Limestone assimilation by basaltic magmas: an experimental re-assessment and application to Italian volcanoes. *Contrib Mineral Petrol* 155:719–738
- Iacono-Marziano G, Morizet Y, Le Trong E, Gaillard F (2012) New experimental data and semi-empirical parameterization of H<sub>2</sub>O–CO<sub>2</sub> solubility in mafic melts. *Geochim Cosmochim Acta* 97:1–23
- Iacovino K, Moore G, Roggensack K, Oppenheimer C, Kyle P (2013) H<sub>2</sub>O–CO<sub>2</sub> solubility in mafic alkaline magma: applications to volatile sources and degassing behavior at Erebus volcano, Antarctica. *Contrib Mineral Petrol*. doi:10.1007/s00410-013-0877-2
- Jakobsson S (1997) Solubility of water and carbon dioxide in an icelandite at 1400°C and 10 kilobars. *Contrib Mineral Petrol* 127:129–135
- Johannes W, Holtz F (1996) Petrogenesis and experimental petrology of granitic rocks. Springer, Berlin
- Kennedy G, Wasserburg G, Heard H, Newton R (1962) The upper three-phase region in the system SiO<sub>2</sub>–H<sub>2</sub>O. *Am J Sci* 260:501
- Kerrick DH, Jacobs GK (1981) A modified Redlick–Kwong equation for H<sub>2</sub>O, CO<sub>2</sub>, and H<sub>2</sub>O–CO<sub>2</sub> mixtures at elevated pressures and temperatures. *Am J Sci* 281:735–767
- Khitrov NI, Kadik AS, Lebedev EB (1963) Estimate of the thermal effect of the separation of water from felsic melts based on data for the system albite–water. *Geochemistry* 7:637–649
- Khitrov NI, Kadik AA, Lebedev YB (1968) solubility of water in a basalt melt. *Geochem Int* 5:667–674
- King PL, Holloway JR (2002) CO<sub>2</sub> solubility and speciation in intermediate (andesitic) melts: the role of H<sub>2</sub>O and composition. *Geochim Cosmochim Acta* 66:1627–1640
- Kogarko LN, Burnham CW, Shettle D (1977) Water regime in alkalic magmas. *Geochem Int* 5:1–8
- Kohn S, Dupree R, Smith ME (1989) A multinuclear magnetic-resonance study of the structure of hydrous albite glasses. *Geochim Cosmochim Acta* 53:2925–2935
- Kress VC, Carmichael ISE (1988) Stoichiometry of the iron oxidation reaction in silicate melts. *Am Mineral* 73:1267–1274
- Kress VC, Carmichael ISE (1991) The compressibility of silicate liquids containing Fe<sub>2</sub>O<sub>3</sub> and the effect of composition, temperature, oxygen fugacity and pressure on their redox states. *Contrib Mineral Petrol* 108:82–92
- Lange RA (1994) The effect of H<sub>2</sub>O, CO<sub>2</sub>, and F on the density and viscosity of silicate melts. In: Carroll MR, Holloway JR (eds) Volatiles in magmas. *Rev Mineral*, vol 30, pp 331–369
- Lange RA, Carmichael ISE (1987) Densities of Na<sub>2</sub>O–K<sub>2</sub>O–CaO–MgO–FeO–Fe<sub>2</sub>O<sub>3</sub>–Al<sub>2</sub>O<sub>3</sub>–TiO<sub>2</sub>–SiO<sub>2</sub> liquids—new measurements and derived partial molar properties. *Geochim Cosmochim Acta* 51:2931–2946
- Larsen J, Gardner J (2004) Experimental study of water degassing from phonolite melts: implications for volatile oversaturation during magmatic ascent. *J Volcanol Geoth Res* 134:109–124
- Lawson CL, Hanson RJ (1974) Solving least squares problems. Prentice-Hall, Englewood Cliffs
- Le Bas MJ, Le Maitre RW, Streckeisen A, Zanettin B (1986) A chemical classification of volcanic rocks based on the total alkali-silica diagram. *J Petrol* 27:745–750
- Lesne P, Kohn SC, Blundy J, Witham F, Botcharnikov RE, Behrens H (2011a) Experimental simulation of closed-system degassing in the system basalt–H<sub>2</sub>O–CO<sub>2</sub>–S–Cl. *J Petrol* 52:1737–1762
- Lesne P, Scaillet B, Pichavant M, Beny J-M (2011b) The carbon dioxide solubility in alkalic basalts: an experimental study. *Contrib Mineral Petrol* 162:153–168
- Lesne P, Scaillet B, Pichavant M, Iacono-Mariziano G, Beny J-M (2011c) The H<sub>2</sub>O solubility of alkali basaltic melts: an experimental study. *Contrib Mineral Petrol* 162:133–151
- Liu Q, Lange RA (2003) New density measurements on carbonate liquids and the partial molar volume of the CaCO<sub>3</sub> component. *Contrib Mineral Petrol* 146:370–381
- Liu Y, Zhang Y, Behrens H (2005) Solubility of H<sub>2</sub>O in rhyolitic melts at low pressures and a new empirical model for mixed H<sub>2</sub>O–CO<sub>2</sub> solubility in rhyolitic melts. *J Volcanol Geoth Res* 143:219–225

- Mangan M, Sisson T (2000) Delayed, disequilibrium degassing in rhyolitic magma: decompression experiments and implications for explosive volcanism. *Earth Planet Sci Lett* 183:441–455
- Martel C, Pichavant M, Bourdier J-L, Traineau H, Holtz F, Scaillet B (1998) Magma storage conditions and control of eruption regime in silicic volcanoes: experimental evidence from Mt. Pelé. *Earth Planet Sci Lett* 156:89–99
- Mattey DP (1991) Carbon dioxide solubility and carbon isotope fractionation in basaltic melt. *Geochim Cosmochim Acta* 55:3467–3473
- Mattey DP, Taylor WR, Green DH, Pillinger CT (1990) Carbon isotopic fractionation between CO<sub>2</sub> vapor, silicate and carbonate melts—an experimental-study to 30 Kbar. *Contrib Mineral Petrol* 104:492–505
- McMillan P, Peraudea G, Holloway J, Coutures JP (1986) Water solubility in a calcium aluminosilicate melt. *Contrib Mineral Petrol* 94:178–182
- Medard E, Grove TL (2008) The effect of H<sub>2</sub>O on the olivine liquidus of basaltic melts: experiments and thermodynamic models. *Contrib Mineral Petrol* 155:417–432
- Métrich N, Rutherford MJ (1998) Low pressure crystallization path of H<sub>2</sub>O-saturated basaltic-hawaiite melts from Mt. Etna: implications for open-system degassing of basaltic volcanoes. *Geochim Cosmochim Acta* 62:1195–1205
- Moore G (2008) Interpreting H<sub>2</sub>O and CO<sub>2</sub> contents in melt inclusions: constraints from solubility experiments and modeling. In: Putirka KD, Tepley FJ III (eds) *Minerals, inclusions and volcanic processes*. *Rev Mineral Geochem*, vol 69, pp 333–361
- Moore G, Carmichael ISE (1998) The hydrous phase equilibria (to 3 kbar) of an andesite and basaltic andesite from western Mexico: constraints on water content and conditions of phenocryst growth. *Contrib Mineral Petrol* 130:304–319
- Moore G, Vennemann T, Carmichael ISE (1998) An empirical model for the solubility of H<sub>2</sub>O in magmas to 3 kilobars. *Am Mineral* 83:36–42
- Moore G, Roggensack K, Klonowski S (2008) A low-pressure high-temperature technique for the piston-cylinder. *Am Mineral* 93:48–52
- Morizet Y, Brooker R, Kohn S (2002) CO<sub>2</sub> in haplo-phonolite melt: solubility, speciation and carbonate complexation. *Geochim Cosmochim Acta* 66:1809–1820
- Morizet Y, Paris M, Gaillard F, Scaillet B (2010) C-O-H fluid solubility in haplobasalt under reducing conditions: an experimental study. *Chem Geol* 279:1–16
- Mysen BO (1976) Role of volatiles in silicate melts—solubility of carbon-dioxide and water in feldspar, pyroxene, and feldspathoid melts to 30 Kb and 1625 °C. *Am J Sci* 276:969–996
- Mysen BO, Cody GD (2004) Solubility and solution mechanism of H<sub>2</sub>O in alkali silicate melts and glasses at high pressure and temperature. *Geochim Cosmochim Acta* 68:5113–5126
- Mysen BO, Seitz MG, Frantz JD (1974) Measurements of the solubility of carbon dioxide in silicate melts utilizing maps of carbon-14 beta activity. *Carnegie Inst Wash Yearb* 73:224–226
- Newman S, Lowenstern JB (2002) VOLATILECALC: a silicate melt-H<sub>2</sub>O–CO<sub>2</sub> solution model written in Visual Basic for excel. *Comput Geosci* 28:597–604
- Nicholls J (1980) A simple thermodynamic model for estimating the solubility of H<sub>2</sub>O in magmas. *Contrib Mineral Petrol* 74:211–220
- Nowak M, Behrens H (1995) Speciation of water in haplogranitic glasses and melts determined by in situ near-infrared spectroscopy. *Geochim Cosmochim Acta* 59:3445–3450
- Nowak M, Schreen D, Spickenbom K (2004) Argon and CO<sub>2</sub> on the race track in silicate melts: a tool for the development of a CO<sub>2</sub> speciation and diffusion model. *Geochim Cosmochim Acta* 68:5127–5138
- Ochs FA III, Lange RL (1997) The partial molar volume, thermal expansivity, and compressibility of H<sub>2</sub>O in NaAlSi<sub>3</sub>O<sub>8</sub> liquid: new measurements and an internally consistent model. *Contrib Mineral Petrol* 129:155–165
- Ohlhorst S, Behrens H, Holtz F (2001) Compositional dependence of molar absorptivities of near-infrared OH<sup>−</sup> and H<sub>2</sub>O bands in rhyolitic to basaltic glasses. *Chem Geol* 174:5–20
- Orlova GP (1962) The solubility of water in albite melts—under pressure. *Int Geol Rev* 6:254–258
- Oxtoby S, Hamilton DL (1978) The discrete association of water with Na<sub>2</sub>O and SiO<sub>2</sub> in NaAl silicate melts. *Contrib Mineral Petrol* 66:185–188
- Paillat O, Elphick SC, Brown WL (1992) The solubility of water in NaAlSi<sub>3</sub>O<sub>8</sub> melts—a reexamination of Ab-H<sub>2</sub>O phase-relationships and critical-behavior at high-pressures. *Contrib Mineral Petrol* 112:490–500
- Pan V, Holloway J, Hervig RL (1991) The pressure and temperature-dependence of carbon-dioxide solubility in tholeiitic basalt melts. *Geochim Cosmochim Acta* 55:1587–1595
- Papale P (1997) Modeling of the solubility of a one-component H<sub>2</sub>O or CO<sub>2</sub> fluid in silicate liquids. *Contrib Mineral Petrol* 126:237–251
- Papale P (1999) Modeling of the solubility of a two-component H<sub>2</sub>O + CO<sub>2</sub> fluid in silicate liquids. *Am Mineral* 84:477–492
- Papale P, Moretti R, Barbato D (2006) The compositional dependence of the saturation surface of H<sub>2</sub>O + CO<sub>2</sub> fluids in silicate melts. *Chem Geol* 229:78–95
- Pawley A, Holloway J, McMillan P (1992) The effect of oxygen fugacity on the solubility of carbon oxygen fluids in basaltic melt. *Earth Planet Sci Lett* 110:213–225
- Persikov ES (1974) Experimental studies of solubility of water in granitic melt and kinetics of the melt-water equilibria at high pressures. *Int Geol Rev* 16:1062–1067
- Pineau F, Shilobreeva S, Kadik A, Javoy M (1998) Water solubility and D/H fractionation in the system basaltic andesite-H<sub>2</sub>O at 1250 °C and between 0.5 and 3 kbars. *Chem Geol* 147:173–184
- Press WH, Teukolsky SA, Vetterling WT, Flannery BP (1999) *Numerical recipes in C: the art of scientific computing*, 2nd edn. Cambridge University Press, Cambridge
- Prigogine I, Defay R (1954) *Chemical thermodynamics*. Longmans Green, New York
- Rai CS, Sharma SK, Muenow DW, Matson DW, Byers CD (1983) Temperature-dependence of CO<sub>2</sub> solubility in high-pressure quenched glasses of diopside composition. *Geochim Cosmochim Acta* 47:953–958
- Roach AL (2005) The evolution of silicic magmatism in the post-caldera volcanism of the Phlegrean Fields, Italy. Ph.D. Dissertation, Brown University
- Robie RA, Hemingway BS, Fisher JR (1978) *Thermodynamic properties of minerals and related substances at 298.15 K and 1 bar (10<sup>5</sup> Pascals) pressure and at higher temperature*. U.S. Geological Survey Bulletin 1452
- Romano C, Dingwell DB, Behrens H (1996) Compositional dependence of H<sub>2</sub>O solubility along the joins NaAlSi<sub>3</sub>O<sub>8</sub>–KAlSi<sub>3</sub>O<sub>8</sub>, NaAlSi<sub>3</sub>O<sub>8</sub>–LiAlSi<sub>3</sub>O<sub>8</sub>, and KAlSi<sub>3</sub>O<sub>8</sub>–LiAlSi<sub>3</sub>O<sub>8</sub>. *Am Mineral* 81:452–461
- Schmidt BC, Behrens H (2008) Water solubility in phonolite melts: influence of melt composition and temperature. *Chem Geol* 256:259–268
- Schmidt B, Holtz F, Pichavant M (1999) Water solubility in haplogranitic melts coexisting with H<sub>2</sub>O–H<sub>2</sub> fluids. *Contrib Mineral Petrol* 136:213–224
- Shaw HR (1963) Obsidian-H<sub>2</sub>O viscosities at 100 and 200 bars in temperature range 700 to 900 °C. *J Geophys Res Solid Earth* 68:6337–6343

- Shishkina TA, Botcharnikov RE, Holtz F, Almeev RR, Portnyagin MV (2010) Solubility of H<sub>2</sub>O- and CO<sub>2</sub>-bearing fluids in tholeiitic basalts at pressures up to 500 MPa. *Chem Geol* 277:115–125
- Shishkina TA, Botcharnikov RE, Holtz F, Almeev RR, Jazwa AM, Jakubiak AA (2014) Compositional and pressure effects on the solubility of H<sub>2</sub>O and CO<sub>2</sub> in mafic melts. *Chem Geol* 388:112–129
- Silver L, Stolper E (1989) Water in albitic glasses. *J Petrol* 30:667–709
- Silver LA, Ihinger PD, Stolper E (1990) The influence of bulk composition on the speciation of water in silicate-glasses. *Contrib Mineral Petrol* 104:142–162
- Spera FJ, Bergman SC (1980) Carbon dioxide in igneous petrogenesis: I. Aspects of the dissolution of CO<sub>2</sub> in silicate liquids. *Contrib Mineral Petrol* 74:55–66
- Spera FJ, Bohron WA, Till CB, Fowler SJ, Ghiorso MS (2007) Partitioning of trace elements among coexisting crystals, melt and supercritical fluid during isobaric fractional crystallization and fractional melting. *Am Mineral* 92:1881–1898
- Stolper EM (1982) The speciation of water in silicate melts. *Geochim Cosmochim Acta* 46:2609–2620
- Stolper EM (1989) Temperature dependence of the speciation of water in rhyolitic melts and glasses. *Am Mineral* 74:1247–1257
- Stolper EM, Holloway JR (1988) Experimental determination of the solubility of carbon dioxide in molten basalt at low pressure. *Earth Planet Sci Lett* 87:397–408
- Tamir N, Behrens H, Holtz F (2001) The solubility of H<sub>2</sub>O and CO<sub>2</sub> in rhyolitic melts in equilibrium with a mixed CO<sub>2</sub>–H<sub>2</sub>O fluid phase. *Chem Geol* 174:333–347
- Thibault Y, Holloway J (1994) Solubility of CO<sub>2</sub> in a Ca-rich leucite—effects of pressure, temperature, and oxygen fugacity. *Contrib Mineral Petrol* 116:216–224
- Vetere F, Botcharnikov RE, Holtz F, Behrens H, De Rosa R (2011) Solubility of H<sub>2</sub>O and CO<sub>2</sub> in shoshonitic melts at 1250 °C and pressures from 50 to 400 MPa: implications for Campi Flegrei magmatic systems. *J Volcanol Geoth Res* 202:251–261
- Vetere F, Holtz F, Behrens H, Botcharnikov RE, Fanara S (2014) The effect of alkalis and polymerization on the solubility of H<sub>2</sub>O and CO<sub>2</sub> in alkali-rich silicate melts. *Contrib Mineral Petrol* 167:1014. doi:10.1007/s00410-014-1014-6
- Wallace PJ, Anderson AT, Davis AM (1995) Quantification of pre-eruptive exsolved gas contents in silicic magmas. *Nature* 377:612–616
- Wallace PJ, Anderson AT, Davis AM (1999) Gradients in H<sub>2</sub>O, CO<sub>2</sub>, and exsolved gas in a large-volume silicic magma system: interpreting the record preserved in melt inclusions from the Bishop Tuff. *J Geophys Res Solid Earth* 104:20097–20122
- Wasserburg GJ (1988) Diffusion of water in silicate melts. *J Geol* 96:363–367
- Watson EB (1979) Diffusion of cesium ions in H<sub>2</sub>O-saturated granitic melt. *Science* 205:1259–1260
- Wilke M, Behrens H, Burkhard D (2002) The oxidation state of iron in silicic melt at 500 MPa water pressure. *Chem Geol* 189:55–67
- Yamashita S (1999) Experimental study of the effect of temperature on water solubility in natural rhyolite melt to 100 MPa. *J Petrol* 40:1497–1507
- Yoder HS Jr (1965) Diopside-anorthite-water at five and ten kilobars and its bearing on explosive volcanism. *Carnegie Inst Wash Yearb* 64:82–89
- Zhang Y, Ni H (2010) Diffusion of H, C and O components in silicate melts. In: Zhang Y, Cherniak J (eds) *Diffusion in minerals and melts*. *Rev Mineral Geochem*, vol 72, pp 171–226